Article

Conformational Complexity and Dynamics in a Muscarinic Receptor Revealed by NMR Spectroscopy

Graphical Abstract
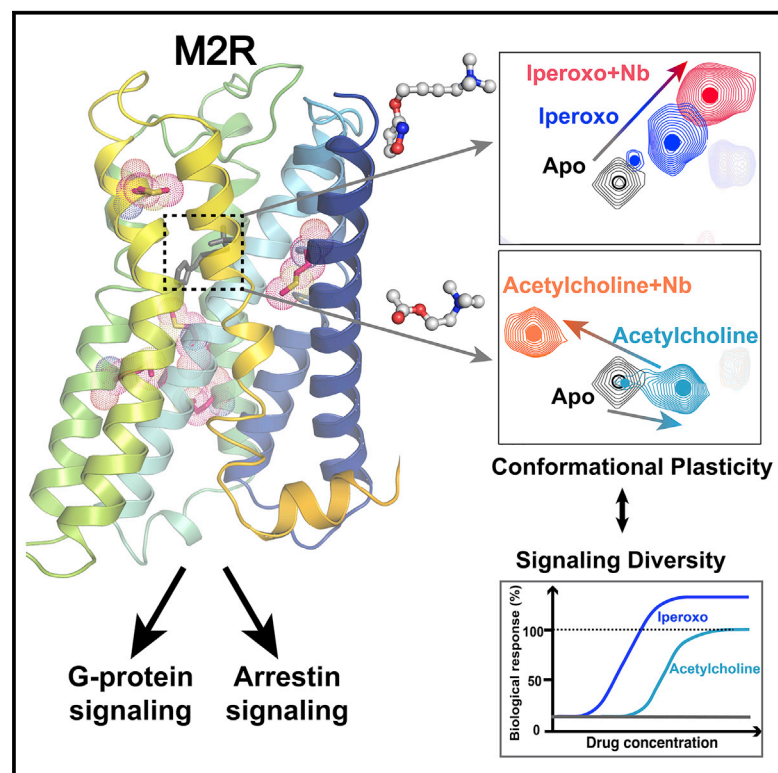
Authors

Jun Xu, Yunfei Hu, Jonas Kaindl, ..., Peter Gmeiner, Changwen Jin, Brian K. Kobilka

Correspondence

changwen@pku.edu.cn (C.J.), kobilka@stanford.edu (B.K.K.)

In Brief

Xu et al. reveal that the M2 muscarinic receptor is highly dynamic, with a complex energy landscape in which ligands with different signaling profiles stabilize distinct receptor conformations.

Highlights

- Analysis of conformational dynamics throughout the M2R using $^{13}CH_3$-ε-methionine NMR

- Ligands with various efficacies for G protein and arrestin signaling were examined

- Each ligand stabilized a distinct conformation of the M2R

- There is no clear linear correlation between ligand efficacy and chemical shifts

CellPress

Molecular Cell
Article

CellPress

Conformational Complexity and Dynamics in a Muscarinic Receptor Revealed by NMR Spectroscopy

Jun Xu,[1] Yunfei Hu,[2,5] Jonas Kaindl,[3] Philipp Risel,[3] Harald Hübner,[3] Shoji Maeda,[4] Xiaogang Niu,[2] Hongwei Li,[2] Peter Gmeiner,[3] Changwen Jin,[2,*] and Brian K. Kobilka[1,4,6,*]

[1]Beijing Advanced Innovation Center for Structural Biology, School of Medicine, Tsinghua University, Beijing 100084, China
[2]Beijing Nuclear Magnetic Resonance Center, College of Chemistry and Molecular Engineering, School of Life Sciences, Peking University, Beijing 100084, China
[3]Department of Chemistry and Pharmacy, Medicinal Chemistry, Friedrich-Alexander-Universität Erlangen-Nürnberg, Nikolaus-Fiebiger-Straße 10, 91058 Erlangen, Germany
[4]Department of Molecular and Cellular Physiology, Stanford University School of Medicine, Stanford, CA 94305, USA
[5]Present address: Medical College of Soochow University, Suzhou 215123, China
[6]Lead Contact
*Correspondence: changwen@pku.edu.cn (C.J.), kobilka@stanford.edu (B.K.K.)
https://doi.org/10.1016/j.molcel.2019.04.028

SUMMARY

The M2 muscarinic acetylcholine receptor (M2R) is a prototypical GPCR that plays important roles in regulating heart rate and CNS functions. Crystal structures provide snapshots of the M2R in inactive and active states, but the allosteric link between the ligand binding pocket and cytoplasmic surface remains poorly understood. Here we used solution NMR to examine the structure and dynamics of the M2R labeled with $^{13}CH_3$-ε-methionine upon binding to various orthosteric and allosteric ligands having a range of efficacy for both G protein activation and arrestin recruitment. We observed ligand-specific changes in the NMR spectra of $^{13}CH_3$-ε-methionine probes in the M2R extracellular domain, transmembrane core, and cytoplasmic surface, allowing us to correlate ligand structure with changes in receptor structure and dynamics. We show that the M2R has a complex energy landscape in which ligands with different efficacy profiles stabilize distinct receptor conformations.

INTRODUCTION

The past decade has seen great advances in the structural biology of G protein-coupled receptors (GPCRs), with more than 50 unique structures reported. Although the majority of structures represent inactive states, the few active-state structures of family A and B GPCRs, including several GPCR-G protein complexes, reveal a common feature of activation: the outward movement of TM6 enabling the engagement with a G protein. Crystal structures of active and inactive states represent relatively stable low-energy conformations and may suggest a simple two-state system;

however, a growing body of evidence from functional and biophysical studies suggests that GPCRs are conformational complex and highly dynamic, with weak allosteric coupling between the agonist binding pocket and the effector coupling interface. NMR studies provide evidence for several distinct conformational states that exchange on millisecond to second timescales for the β2AR, the μOR, and the A2A adenosine receptor (Nygaard et al., 2013; Sounier et al., 2015; Ye et al., 2016).

Muscarinic receptors (M1–M5) are prototypical family A GPCRs that mediate responses to acetylcholine (ACh) in both the CNS and peripheral nervous system (van Koppen and Kaiser, 2003). These receptors are attractive therapeutic targets for treatment of a diverse range of pathophysiological conditions, including Parkinson's disease, Alzheimer's disease, and cardiovascular disease (Conn et al., 2009; Wess et al., 2007). Muscarinic receptors, particularly the M2R subtype, have long served as important model systems in GPCR biology and pharmacology because of their regulation by both orthosteric and allosteric ligands (Gregory et al., 2007). Crystal structures of M2R have been determined in both inactive and active states, as well as an active structure bound to a positive allosteric modulator (Haga et al., 2012; Kruse et al., 2013). Like many GPCRs, the M2R exhibits ligand-specific signaling preferences for G protein and arrestin pathways, as well as a range of ligand efficacies (inverse agonists to full agonists) for these pathways. This complex behavior could be explained by ligands' differentially stabilizing a limited number of conformations (a simple two- or three-state system) or by each ligand's stabilizing a distinct receptor conformation. To investigate the structural basis for these ligand-specific behaviors, we used solution nuclear magnetic resonance (NMR) to monitor the chemical environment around five $^{13}CH_3$-ε-methionines located in different structure regions of M2R in response to a spectrum of ligands. These NMR studies, in combination with functional analysis and molecular dynamics (MD) simulations, reveal that the M2R is highly dynamic, with a complex energy landscape

CellPress
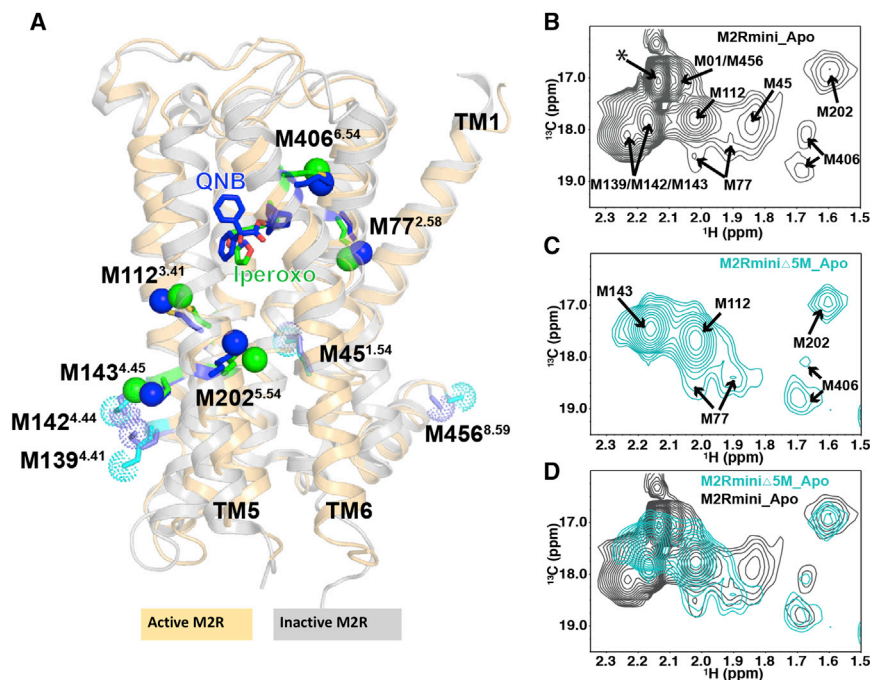
Figure 1. Modified M2R for NMR and Spectra Assignment

(A) Methionines in the inactive (PDB: 3UON) and active (PDB: 4MQS) M2R crystal structures. Solid spheres shown in green (active) and blue (inactive) represent the methionine methyl carbon left in M2Rmini$_\Delta$5M, whereas dotted spheres shown in cyan (active) and slate (inactive) represent methyl carbon of methionines mutated to other residues.

(B and C) Assignment of the HSQC spectra of apo-state M2Rmini (B) and M2Rmini$_\Delta$5M (C). Asterisk represents overlapped signal from M01, M139, M142, M143, and M456.

(D) Superimposed spectra of apo-state M2Rmini and M2Rmini$_\Delta$5M. The overall chemical shifts of the retained 5 methionines are nearly unchanged. See also Figures S1–S4.

creases the hydrodynamic radius of the receptor and reduces the quality of the spectra. We therefore used M2Rmini$_\Delta$5M for further NMR studies. The retained five methionines are all in the transmembrane bundle of M2R and are well positioned to detect the confor-mational changes throughout the receptor (Figures 1A and S1A–S1F).

in which every ligand stabilizes a different set of con-formations, providing new structural insights into ligand efficacy and bias.

RESULTS

Chemical Shift Assignments for $^{13}CH_3$-ε-Methionine-Labeled M2R

There are ten methionines in the M2R construct that was used for crystallographic studies (Kruse et al., 2013) in which ICL3 has been deleted, referred to as M2Rmini (Figures 1A and S1A–S1G). Five of them, M77$^{2.58}$, M112$^{3.41}$, M202$^{5.54}$, M143$^{4.45}$, and M406$^{6.54}$ (Ballesteros-Weinstein numbering), are highly conserved in muscarinic family GPCRs (Figure S1H). The purified M2Rmini is highly stable and maintains its function for the duration of the NMR experiments (Figures S1I and S1J). The $^{13}CH_3$-ε-methionine resonances in the two-dimensional (2D) ^1H-^{13}C heteronuclear single quantum coherence (HSQC) spectra of M2Rmini were assigned through combinatorial mutagenesis as described in Figures S2, S3, and S4. To over-come the problem of peak overlap, we introduced the following mutations to generate the construct referred to as M2Rmini$_\Delta$5M (Figure S1G): M01T, M45L, M139L, M142L, and M456T. The HSQC spectra of M2Rmini$_\Delta$5M are remarkably simplified, and the chemical shifts of the remaining residues are nearly the same as in the M2Rmini (Figures 1B–1D), indicating that these mutations do not affect the overall structure of M2R. The spectra of M2Rmini$_\Delta$5M are similar to those of M2RFL$_\Delta$5M, which has an intact ICL3 (Figure S4C), and the functional prop-erties of M2Rmini$_\Delta$5M are also similar to those of the M2RFL_WT (Figure S1K). These results suggest that the ICL3 deletion has little effect on the conformation of the receptor's transmembrane region. However, because of its size, ICL3 in-

Ligand-Specific Conformations Monitored by the HSQC Spectra of M2R

To investigate the effect of ligand structure on the conforma-tion and dynamics of M2R, we selected a series of structurally distinct ligands (Figure 2A), including four antagonists (QNB, tiotropium, scopolamine, and gallamine) and six agonists (xanomeline, pilocarpine, ACh, carbachol, iperoxo, and PR15). Gallamine is a well-characterized allosteric modulator of M2R that reduces binding affinity of [^3H]NMS and exhibits antagonism on its own at higher concentration (Figure S1K; Gregory et al., 2007). We measured the efficacies of each agonist toward G protein and β-arrestin using cell-based as-says (Figures 2B–2E). The functional results show that xano-meline and pilocarpine are two partial agonists relative to ACh for both G protein activation and β-arrestin recruitment (Figures 2B and 2C), and both are more biased toward G protein activation, particularly xanomeline (Figure 2E). Consistent with the similar chemical structures, ACh and carbachol have almost identical functional properties and are set as full agonists in this study. Iperoxo is a synthetic high-affinity agonist that was used to obtain the active M2R crystal structure (Kruse et al., 2013). Instead of the acetyl group of ACh, iperoxo has an isoxazoline ring, whereas the C-N double bond of the ring formally replaces the C = O unit of ACh. Additionally, an acetylene moiety has been in-serted between the cationic nitrogen and the acetyl-simulating isoxazoline ring. It has been reported that iperoxo is more efficacious than ACh, and it is classified as a super-agonist (Langmead and Christopoulos, 2013). Indeed, we observe that iperoxo is more efficacious than ACh for β-arrestin

Figure 2. Ligands Used in this Study and Functional Properties of Agonists

(A) Chemical structures of ligands used in this study. The structural differences among QNB, tiotropium, and scopolamine are highlighted with yellow and green boxes.

(B and C) Concentration-response curves of different agonists toward β-arrestin-2 recruitment (B) and G protein activation (C) measured by the PathHunter assay and a cell-based Gqi-inositol phosphate accumulation assay, respectively. Data are presented as mean ± SEM of four to ten independent experiments with repeats in duplicate.

(D) Efficacies of different agonists toward GTP hydrolysis activity measured by GTPase Glo assay using purified M2R and GoA. For all three assays, the data were normalized to the percentage maximal response for ACh and are presented as mean ± SEM of three independent experiments with repeats in triplicate.

(E) The efficacy (Emax; percentage of ACh) values and signaling bias parameters ($_\Delta\log[\tau/KA]$, $_{\Delta\Delta}\log[\tau/KA]$, and bias factor) are presented across functional assays. The calculation details for signaling bias parameters are described in STAR Methods. Statistical analysis was performed using a two-tailed unpaired Student's t test on the $_\Delta\log(\tau/K_A)$ ratios (mean, SEM, n) to make comparisons between two pathways (G protein activation and β-arrestin recruitment) of for each ligand. p values < 0.05 were considered to indicate statistical significance.

| | β-Arr | | Gqi | | Gqi/β-Arr | | Glo™-assay |
	E_{max}(% ACh)	$\triangle\log(\tau/K_A)$	E_{max}(% ACh)	$\triangle\log(\tau/K_A)$	$\triangle\triangle\log(\tau/K_A)$	Bias factor	Efficacy (% ACh)
Acetylcholine	100	0.00±0.07	100	0.00±0.06	0.00±0.10	1.00	100.0
Iperoxo	145±3	2.91±0.06	107±3	2.67±0.06	−0.24±0.08	0.57*	139.3±11.6
Pilocarpine	52±1	−1.66±0.09	67±6	−1.32±0.09	0.34±0.13	2.18*	68.9±3.3
Xanomeline	44±1	−1.23±0.10	67±4	0.24±0.09	1.47±0.13	29.42*	87.1±2.8
PR15	98±2	−0.16±0.07	111±2	0.32±0.06	0.48±0.09	2.98*	139.4±11.9
Carbachol	87±1	−0.28±0.07	100±2	−0.34±0.06	−0.06±0.09	0.88	98.2±2.8

*P<0.05 was considered to be statistically significant (determined on the $\triangle\log(\tau/K_A)$ level between the two pathways for each ligand).

recruitment (145% of ACh) and G protein activation (107% of ACh) (Figures 2B–2E). Because the super-efficacy of iperoxo toward G protein activation is relatively small in the IP-1 assay, we further confirmed this observation by the GTPase Glo assay using purified M2R and GoA (139% of ACh; Figures 2D and 2E). PR15 is a synthetic agonist that is structurally a hybrid of iperoxo and ACh (Figure 2A; Bebbington et al., 1966), having the acetylene component, but not the isoxazoline ring. Of interest, PR15 exhibits super-efficacy toward G protein activation but not β-arrestin recruitment (Figures 2B–2E).

We then collected a series of HSQC spectra of M2Rmini$_\Delta$5M bound to each ligand (Figures 3A–3J). In addition, we acquired the HSQC spectra of M2Rmini$_\Delta$5M bound to each agonist in the presence of the G protein-mimetic nanobody Nb9-8 except for xanomeline (Figures 3K–3O); when bound to xanomeline, the receptor failed to form a biochemically stable complex with Nb9-8. Surprisingly, we observed distinct HSQC spectra for each ligand and that the intracellular binding partner Nb9-8 can further alter the spectra of agonist-

bound receptors (Figures 3K–3O and S5A–S5F). We now focus our analysis on the five individual methionines located at three different regions of the receptor: the extracellular ligand binding domain (M77$^{2.58}$ and M406$^{6.54}$), the transmembrane core of TM3 (M112$^{3.41}$), and the G protein coupling domain (M143$^{4.45}$ and M202$^{5.54}$).

Ligand-Dependent Conformational Changes around the Orthosteric and Allosteric Binding Sites

Muscarinic receptors possess a large extracellular vestibule, which is the binding pocket for a number of allosteric modulators (Dror et al., 2013; Kruse et al., 2013). Comparison of inactive and active structures of M2R show obvious conformational changes in both the orthosteric pocket and the allosteric vestibule (Figures 4A and 4B), with a network of aromatic residues connecting the orthosteric and allosteric pockets rearranged (Figure 4C). M77$^{2.58}$ and M406$^{6.54}$ are ideally placed at opposite ends of the aromatic network (Figure 4C). The chemical environment around the ε-methyl group of M77$^{2.58}$ and M406$^{6.54}$ could be strongly influenced by conformational changes of the surrounding aromatic residues because of their ring current effects (Wishart, 2011). Moreover, both M77$^{2.58}$ and M406$^{6.54}$ are at least 7 Å away from the bound ligands, as revealed by the QNB or iperoxo-bound crystal structures, so the ligand chemistry should have little direct
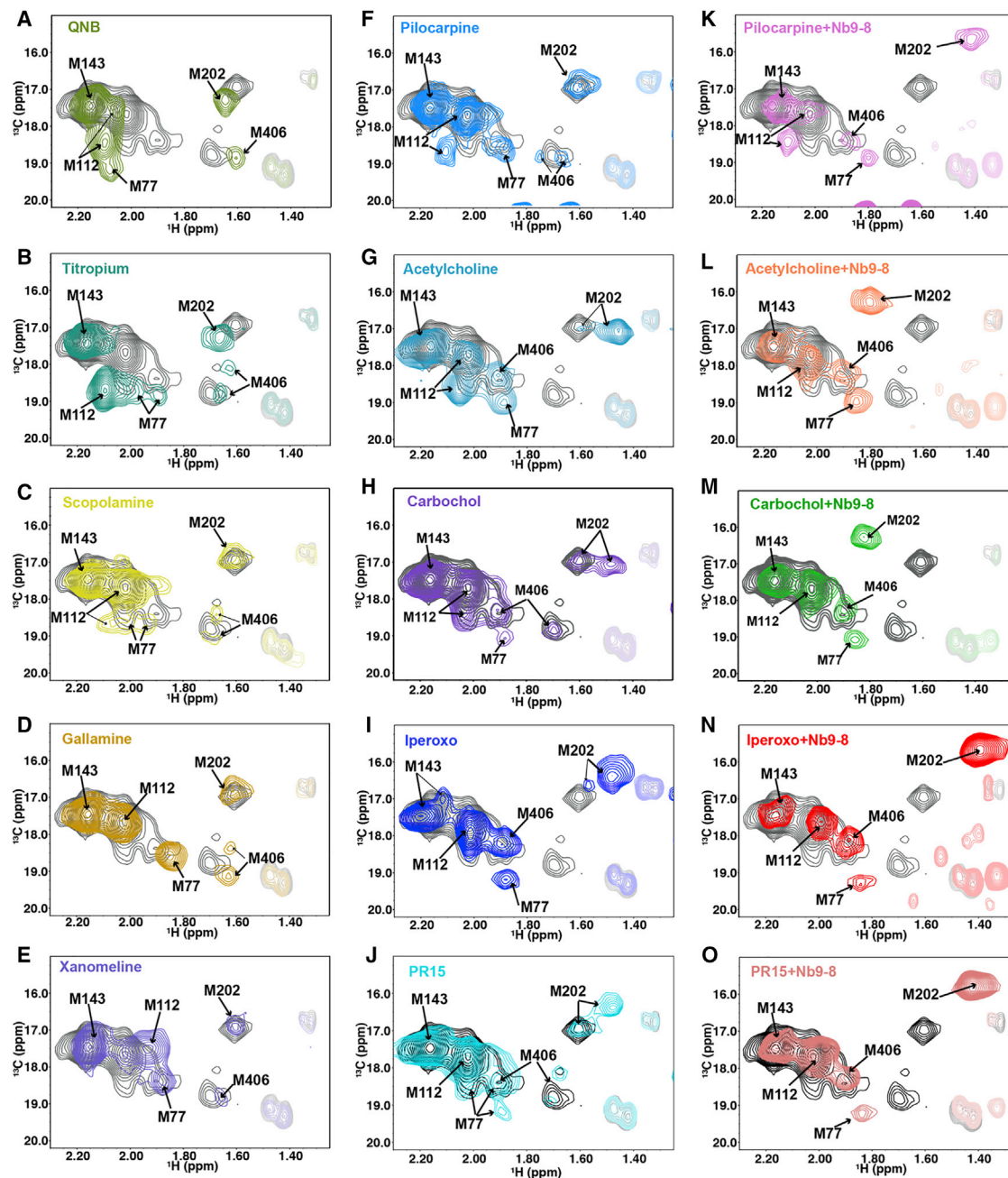
Figure 3. Ligand-Specific Effects on the Overall HSQC Spectra of M2Rmini_Δ5M

Overall HSQC spectra of M2Rmini_Δ5M bound to antagonists QNB (A), titropium (B), scopolamine (C), gallamine (D); agonists xanomeline (E), pilocarpine (F), acetylcholine (G), carbochol (H), iperoxo (I), PR15 (J); and agonists together with Nb9-8: pilocarpine+Nb9-8 (K), acetylcholine+Nb9-8 (L), carbochol+Nb9-8 (M), iperexo+Nb9-8 (N), and PR15+Nb9-8 (O). In gray, the apo-state spectrum is set as a reference. For clarity, signals that are not assigned are shown as transparent. See also Figure S5.

effect on their chemical shifts (Kofuku et al., 2012). Thus, the NMR spectral changes of M77$^{2.58}$ and M406$^{6.54}$ should report on the ligand-dependent conformational changes of M2R orthosteric site and allosteric vestibule. As expected, the NMR cross-peaks of both M77$^{2.58}$ and M406$^{6.54}$ in the HSQC spectra are highly dependent on the bound ligands (Figures 4D and 4E), suggesting that each ligand stabilizes specific conformational changes.

Moreover, we observe long-range allosteric modulation of the local environments of M77$^{2.58}$ and M406$^{6.54}$ upon binding of Nb9-8 to the intracellular side of M2R (Figures 4F and 4G).

For apo-M2R, both M77$^{2.58}$ and M406$^{6.54}$ show two peaks, suggesting the existence of at least two distinct conformations. Upon binding to antagonists, chemical shift changes were observed for both M77$^{2.58}$ and M406$^{6.54}$, suggesting perturbation of the local
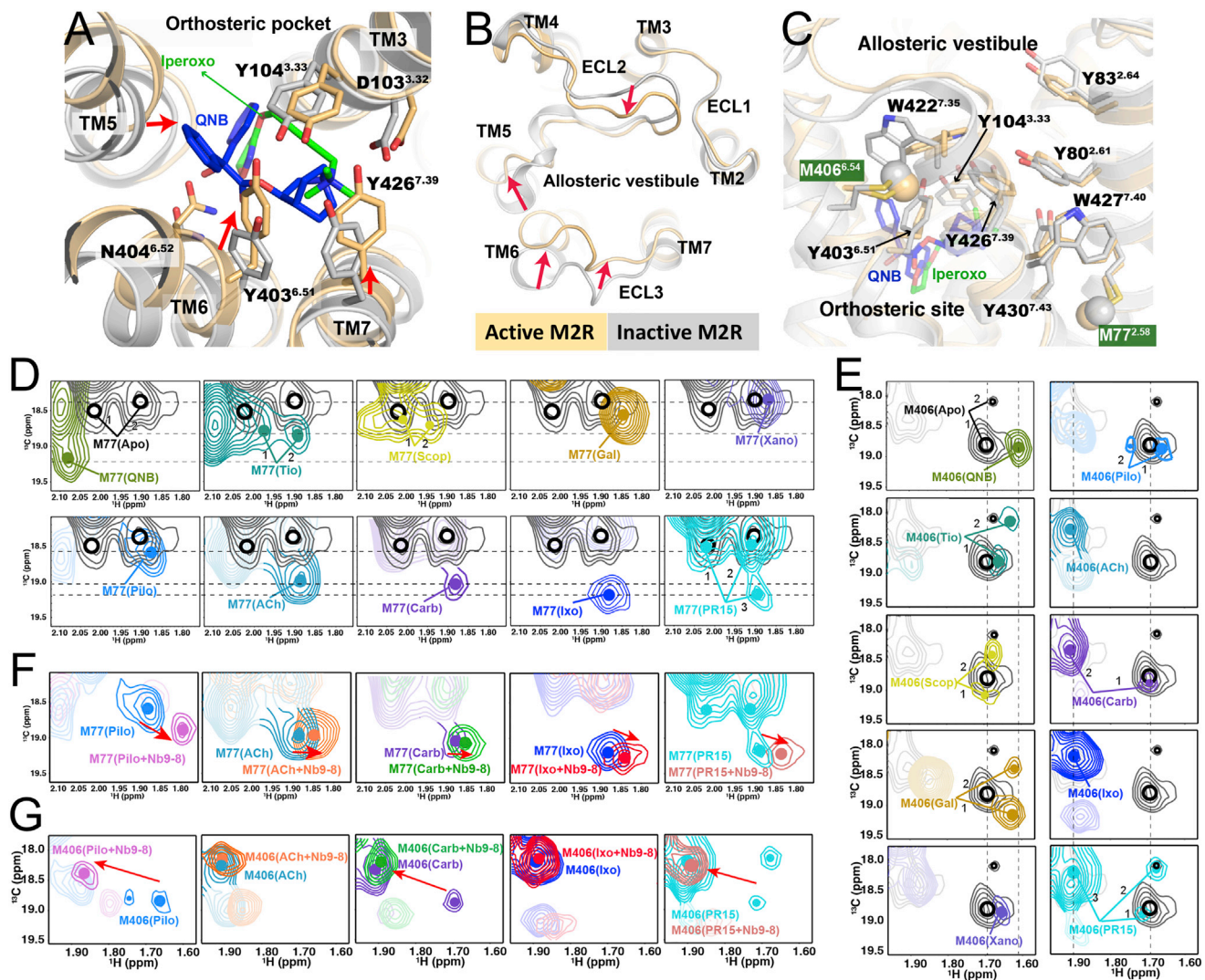
Figure 4. Ligand-Dependent Spectral Changes for Extracellular Residues M77$^{2.58}$ and M406$^{6.54}$

(A and B) Conformational changes in the orthosteric pocket (A) and the extracellular vestibule (B) in the inactive and active structures of M2R. Red arrows indicate the structural changes upon receptor activation. The antagonist QNB (blue) and agonist iperoxo (green) are shown as sticks.

(C) The rearrangement of the aromatic network upon receptor activation could change the chemical environment surrounding M77$^{2.58}$ and M406$^{6.54}$.

(D and E) The HSQC spectra of M77$^{2.58}$ (D) and M406$^{6.54}$ (E) bound to different ligands.

(F and G) Effects of Nb9-8 on the agonist-bound spectra of M77$^{2.58}$ (F) and M406$^{6.54}$ (G). Red arrows indicate the chemical shift changes upon binding with Nb9-8. For clarity, signals from other residues are shown as transparent. The peak centers for apo-state spectra are shown as black circles, and the peak centers in ligand-bound spectra are shown as colored dots. The multiple peaks in each corresponding state are labeled with Arabic numerals. See also Figure S5.

chemical environments. However, the observed peak numbers as well as peak positions show more conformational heterogeneity for tiotropium- and scopolamine-bound receptors compared with QNB-bound receptor (Figures 4D and 4E). These results suggest that tiotropium or scopolamine does not stabilize the extracellular domain of M2R in the same conformation as QNB, which is consistent with the observation that residues D$^{3.32}$, Y$^{7.39}$, and Y$^{7.43}$ show different rotamers in the crystal structure of QNB-bound M2R compared with those of NMS-bound M3R and tiotropium-bound M4R (Figures S5G and S5H). The observed difference may be attributed to the unique quinuclidine group of QNB compared with the bulky scopine group in tiotropium and NMS

structures (Figure 2A, yellow box). Despite the relatively low binding affinity (Figure S1K), gallamine apparently stabilizes the extracellular domain of M2R in a distinct conformation, in which M406$^{6.54}$ still shows two peaks while M77$^{2.58}$ is stabilized in a single well-shaped peak with increased intensity and with chemical shifts dissimilar to those observed in other antagonist-bound states (Figures 4D and S5A). Intriguingly, previous MD simulations study showed that gallamine binds to the extracellular vestibule of M2R, and one of the ammonium group forms direct cation-π interactions with Y80$^{2.61}$ and Y83$^{2.64}$ (Dror et al., 2013), which may stabilize a more uniform conformation at the extracellular end of TM2 and explain the observation of a single peak for M77$^{2.58}$.

CellPress

Agonist binding changes the NMR signal of M77$^{2.58}$ and M406$^{6.54}$ in a distinct pattern. Binding of full agonists ACh and carbochol or super-agonists iperoxo and PR15 to M2R stabilizes significant conformational changes in the extracellular domain, as evidenced by the appearance of a strong, well-shaped peak for M406$^{6.54}$ that is shifted ~0.2 ppm downfield in the ^{1}H dimension compared with the apo form (Figure 4E). Notably, the direction of the peak shifts when binding to full or super-agonists is opposite to that of antagonists. This may reflect the fact that TM6 moves as a rigid body upon activation, with the cytoplasmic end moving outward and the extracellular end moving inward (Figure 4A). For M77$^{2.58}$, significant chemical shift changes were also observed, while the extent of peak shifts varies between the full and super-agonists (Figure 4D), suggesting that the surrounding conformational environment is slightly different when bound to the two classes of agonists. Note that when bound to carbachol or PR15, we still observe apo-like peaks for M406$^{6.54}$. In particular, both M77$^{2.58}$ and M406$^{6.54}$ show at least three sets of peaks in the PR15-bound state, indicating a much more complex conformational equilibrium in which the active and apo-like forms simultaneously exist.

In contrast to full agonists, binding of partial agonists xanomeline and pilocarpine cause only small chemical shift changes for both M77$^{2.58}$ and M406$^{6.54}$ signals. For M77$^{2.58}$, it is interesting to notice that the peak position of xanomeline- or pilocarpine-bound state is close to one of the two peaks in the apo-form and shifts slightly, whereas it progressively shifts further in the ACh- or carbachol-bound form and finally to the "fully activated" form when bound to super-agonists. For M406$^{6.54}$, however, binding of partial agonists results in the loss of signal intensity (e.g., bound to xanomeline) or multiple peaks (e.g., bound to pilocarpine) with smaller chemical shift changes, both suggesting that the local conformation may become more dynamic and sample two or more conformations that exchange on the intermediate or slow NMR timescales. The distinct effects between partial and full or super-agonists may be due to their different chemotypes (Figure 2A). The two bulky ring groups of xanomeline and pilocarpine are more similar to antagonists and may be less efficient in stabilizing the active conformation in the extracellular domain, because they would prevent Y104$^{3.33}$, Y403$^{6.51}$, and Y426$^{7.39}$ from forming a lid over the orthosteric pocket (Figure 4A).

Binding of Nb9-8 at the cytoplasmic surface of M2R leads to further changes in the NMR resonances of M77$^{2.58}$ and M406$^{6.54}$ (Figures 4F and 4G). Particularly, Nb9-8 helps stabilize the carbachol and PR15-bound M406$^{6.54}$ peaks into one single peak and causes an obvious shift of M406$^{6.54}$ peak in pilocarpine-bound M2R toward the positions observed for other agonists. These results reflect further structural changes in the orthosteric pocket and the allosteric vestibule, which may correspond to the formation of fully active conformation, in agreement with the allosteric effect of Nb9-8 enhancing agonist binding affinity (Kruse et al., 2013).

Ligand-Dependent Conformational Dynamics of the Transmembrane Core

Despite the increasing number of inactive and active-state GPCR structures, the mechanism by which the ligand-stabilized conformational changes in the orthosteric pocket propagate into the G protein coupling domain is still unclear. Previous MD simulations studies on β2AR found that the connector region, which consists of the core domain of TM3, TM5, and TM6, may be key for the conformational propagation (Dror et al., 2011). The recent active-state structure of μ-opioid receptor (μOR), the β2AR (Huang et al., 2015; Rasmussen et al., 2011), and the A2A receptor (Carpenter et al., 2016) also reveal conserved structural rearrangements in this core triad consisting of I$^{3.40}$, P$^{5.50}$, and F$^{6.44}$ between inactivate and active states (Figure 5A). However, the triad consists of V$^{3.40}$, P$^{5.50}$, and F$^{6.44}$ in the M2R, the smaller side chain of V$^{3.40}$ packs loosely against P$^{5.50}$ and F$^{6.44}$, and there is little rearrangement upon activation. Despite this, a recent study of inactive- and active-state family A GPCR structures, including the M2R, using interhelical interaction-based analysis suggests that the TM3 core domain (3.40–3.43) may act as a key allosteric hub in propagating conformational changes from the orthosteric pocket to the cytoplasmic surface (Lans et al., 2015). Crystal structures of M2R show that the upper part of TM3 contains key residues that form the orthosteric binding pocket, and M112$^{3.41}$ is just located in allosteric hub of TM3 (Figure 5B). Our NMR data show significant ligand-dependent spectral changes of M112$^{3.41}$, and in agreement with the loosely packed triad, we observed substantial conformational heterogeneity in this region.

As shown in Figures 5C and S5C, M112$^{3.41}$ displays a single strong peak in the apo-M2R spectrum, indicating a relatively uniform local conformation. Similar to what is observed in the extracellular region, we also observed different M112$^{3.41}$ spectra for tiotropium, QNB, and scopolamine, suggesting that these antagonists stabilize different conformations of TM3. Gallamine was reported to bind in the allosteric site of the M2R and have little contact with TM3 (Dror et al., 2013). Consistent with this binding mode, it has little effect on the spectrum of M112$^{3.41}$.

Upon binding to agonists, we observe substantial slow to intermediate conformational exchanges (Figure 5C). A distinct chemical shift for M112$^{3.41}$ in the xanomeline-bound state is observed, which is quite different from the other agonists, and the peak is apparently broadened in ^{1}H dimension compared with the apo-state (Figure S6A). Recall that xanomeline is the most G protein-biased agonist (Figure 2E). The line-broadening phenomenon usually indicates exchanges between multiple conformations on the intermediate NMR timescale (microseconds to milliseconds) (Mittermaier and Kay, 2009). When pilocarpine or ACh is bound, two separate peaks are observed for M112$^{3.41}$, one of them shifted downfield of the apo state. This observation suggests the existence of multiple conformational states around the TM3 core domain that might be in slow exchange with each other. Despite the similar chemical structure, the two peaks of M112$^{3.41}$ in the carbachol-bound state are closer to each other compared with that of ACh-bound state, indicating that carbachol stabilizes slightly different conformations than ACh and that the two conformations in carbachol bound state are more similar to each other. Although we do not observe separate peaks for the iperoxo-bound state, the M112$^{3.41}$ peak shifts slightly downfield and also shows decreased peak intensity and a slightly
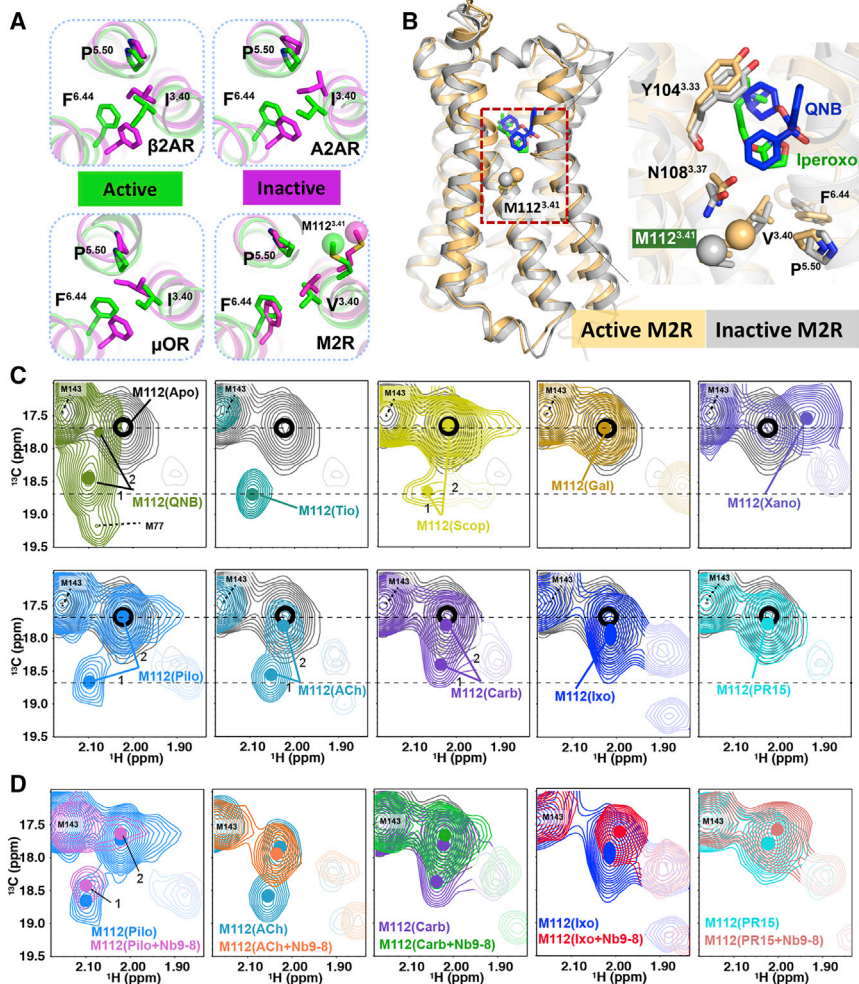
Figure 5. Ligand-Dependent Spectral Changes for the TM3 Core Domain Residue M112$^{3.41}$

(A) The structural rearrangements of the core triad in the inactive and active structures of β2AR, A2AR, and μOR and M2R. The three conserved residues I$^{3.40}$, P$^{5.50}$, and F$^{6.44}$ are shown as sticks.

(B) M112$^{3.41}$ is located at the transmembrane core of M2R that links the extracellular and intracellular domains. Residues in TM3 that have direct or potential interactions with the antagonist QNB or agonist iperoxo and the P$^{5.50}$-V$^{3.40}$-F$^{6.44}$ motif residues are shown as sticks.

(C) The HSQC spectra of M112$^{3.41}$ bound to different ligands.

(D) Effects of Nb9-8 on the agonist-bound spectra of M112$^{3.41}$.

See also Figures S5 and S6.

of Nb9-8 stabilizes M112$^{3.41}$ in a more uniform conformation, as evidenced by a single peak as shown in Figure 5D. In contrast, M112$^{3.41}$ still shows two separate weak peaks when bound to pilocarpine in the presence of Nb9-8, indicating that multiple conformations exist in the ternary complex. Taken together, the ligand-specific spectral changes of M112$^{3.41}$ as well as the modulation by Nb9-8 suggest that TM3 core domain plays important roles in the conformational coupling between ligand binding site and the G protein coupling site. Of interest, these data are consistent with the recent discovery that certain allosteric modulators bound to this region can affect orthosteric ligands binding and downstream signaling (Liu et al., 2018).

elongated shape in the ^{13}C dimension (Figure S6B). We therefore suspect that there are probably two overlapping peaks. Unexpectedly, the hybrid agonist PR15 shows the smallest perturbation on M112$^{3.41}$. Taken together, these results suggest that agonist binding can lead to slow to intermediate conformational exchanges in the TM3 core domain. It is possible that pilocarpine, ACh, carbachol, iperoxo, and PR15 all stabilize the same two conformations but with different exchange rates, where the more rapid exchange rates would lead to movement of the two peaks closer to each other. It is also possible that each agonist is stabilizing a distinct conformation. Of note, the two super-agonists for G protein activation show the smallest spectral changes relative to the apo state, and there is no clear correlation of peak position with ligand efficacy, as would be expected with a simple two-state model of receptor activation.

We also observed effects of Nb9-8 binding on the M112$^{3.41}$ signal in an agonist-dependent manner (Figure 5D). The addition of Nb9-8 leads to relatively small changes in the chemical shift for M2R bound to iperoxo and PR15 and shifts the spectra of M2R bound to ACh and carbachol to a position similar to that for iperoxo. For all four agonists, the addition

Ligand-Dependent Conformational Changes in the G Protein Binding Domain

In contrast to the structural diversity of the binding pocket and extracellular surface of family A GPCRs, the overall structural changes upon activation in G protein coupling interface are similar. M2R activation is characterized by the rearrangement of the intracellular ends of TMs 5, 6, and 7, of which most notable is the outward movement of TM6 and a water-mediated hydrogen bond of Y206$^{5.58}$ and Y440$^{7.53}$ (Figure 6A; Huang et al., 2015; Kruse et al., 2013). M202$^{5.54}$ is ideally positioned to detect these structural changes.

As shown in Figure 6C, QNB and tiotropium shift the M202$^{5.54}$ peak significantly downfield from the apo state, while scopolamine and gallamine have smaller effects on the peak position. The difference between scopolamine and tiotropium or QNB may be attributed to differences in ligand structures. Tiotropium and QNB have two arene rings, while scopolamine has only one (Figure 2A, green box). On the basis of the crystal structure of the M3R bound to NMS, we could predict that scopolamine bound
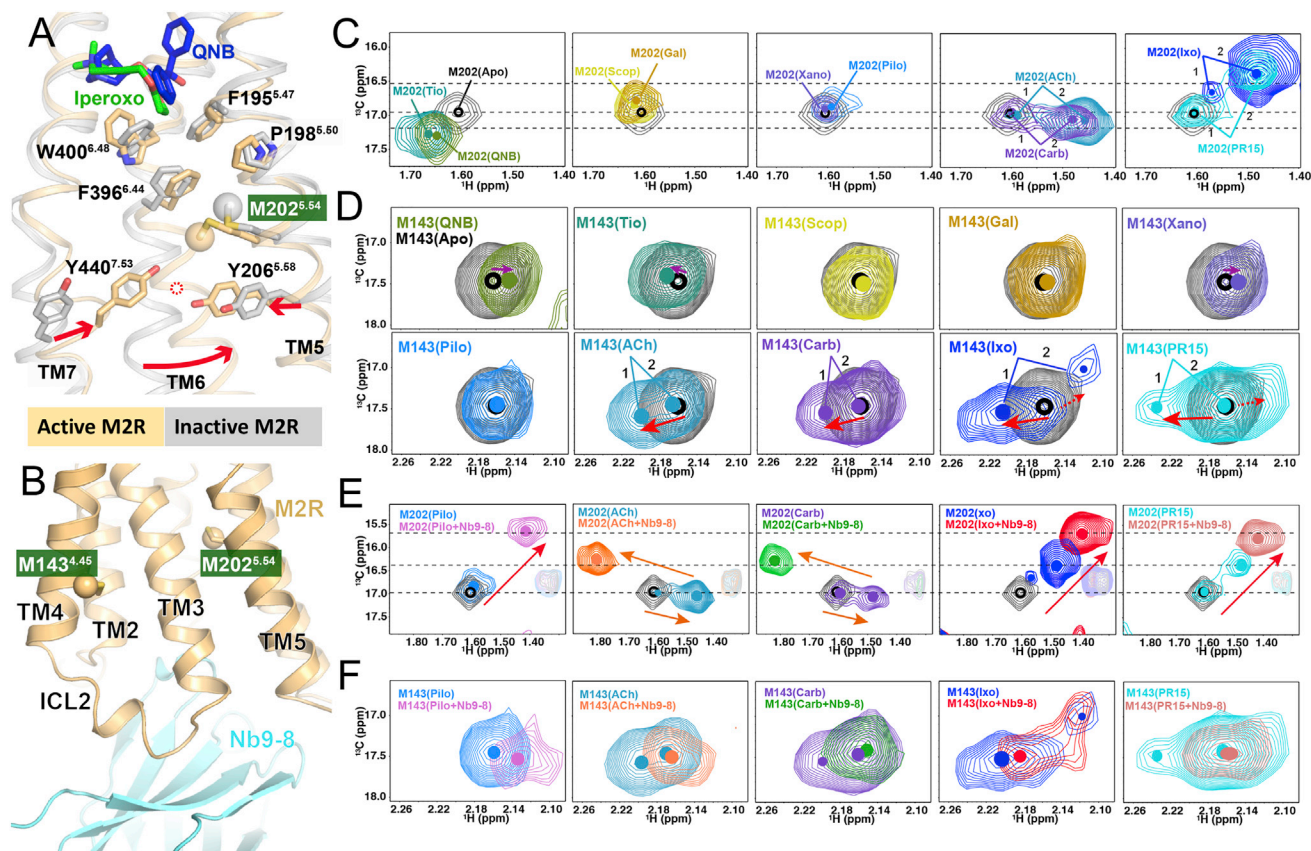
Figure 6. Ligand-Dependent Spectral Changes for Intracellular Residues M202$^{5.54}$ and M143$^{4.45}$

(A) Location of M202$^{5.54}$ and the conformational changes of TM5, TM6, and TM7 upon M2R activation (red arrows). M202$^{5.54}$ and the surrounding conserved residues are shown as sticks. The red dashed circle represents the putative water molecular, which was identified in the crystal structure of µOR (Huang et al., 2015).

(B) Active M2R crystal structure shows that TM4 and TM5 have no interaction with Nb9-8 and that the chemical environments of M202$^{5.54}$ and M143$^{4.45}$ will not be affected by Nb9-8 itself.

(C and D) The spectra of M202$^{5.54}$ (C) and M143$^{4.45}$ (D) bound to different ligands.

(E and F) Effects of Nb9-8 on the agonist-bound spectra of M202$^{5.54}$ (E) and M143$^{4.45}$ (F). Arrows indicate the trend of chemical shift changes during the activation process.

See also Figures S5 and S6.

to the M2R would lack an aromatic interaction with TM5 and TM6 (Figure S5H, blue circle). Of interest, binding of the partial agonist xanomeline or pilocarpine results in only small changes in the M202$^{5.54}$ peak position (Figure 6C). In contrast to the partial agonists, the full agonist ACh and carbachol shifts M202$^{5.54}$ significantly upfield in the ^{1}H dimension, indicating larger structural changes than the partial agonists. Surprisingly, the chemical shifts of M202$^{5.54}$ for iperoxo and PR15 differs significantly from ACh and carbachol, suggesting that the two classes of agonists stabilize distinct conformational changes in TM5 and TM6. For both classes of agonists, we observe two peaks for M202$^{5.54}$, one being very close to the apo-state peak. This indicates the co-existence of at least two different conformations of the TM5-TM6 interface that may be in slow exchange with each other when a full or super-agonist is bound. Although only one major peak for M202$^{5.54}$ was observed in xanomeline- and pilocarpine-bound spectra, these peaks appear to be more distorted or with lower intensities than the apo-M2R spectrum, sug-

gesting intermediate conformational exchanges in this region (Figure S6C).

Despite the insignificant structural changes surrounding ε-methyl of M143$^{4.45}$ on the basis of the crystal structures (Figures 1A and S1F), we observed agonist-dependent conformational dynamics around M143$^{4.45}$, as evidenced by changes in its NMR spectra. To improve spectral resolution and better observe the signal changes of M143$^{4.45}$, we processed the data using a sine-bell window function and an additional Lorentz-to-Gauss window function in the ^{1}H dimension (see Figure S6E for data processed using the normal method). As shown in Figure 6D, binding of QNB and tiotropium causes the M143$^{4.45}$ peak to shift slightly, while scopolamine and gallamine hardly perturb M143$^{4.45}$, suggesting minimal changes in conformation or dynamics in this region. The two partial agonists also seem to have little perturbation on M143$^{4.45}$ chemical shift, although they do decrease the intensities of M143$^{4.45}$ to some extent, suggesting that this region may gain certain dynamics on the

intermediate NMR timescale (Figure S5E). When a full or super-agonist is bound, we observe the appearance of multiple peaks, one of which shifts downfield from the apo-state peak (Figure 6D, red arrows), suggesting significant structural changes and the existence of multiple conformations. Notably, there is an additional new peak shifting upfield when bound to iperoxo (Figure 6D, red arrow), and a similar situation may also hold true for PR15, suggesting that the super-agonists induce more complex conformational dynamics surrounding M143$^{4.45}$ than ACh and carbachol.

The results from M202$^{5.54}$ and M143$^{4.45}$ when taken together show that agonists binding can lead to distinct conformational sub-states in the cytoplasmic domain and that full or super-agonists can stabilize larger and more complex structural changes than partial agonists. The smaller structural changes caused by xanomeline and pilocarpine in the G protein coupling domain are consistent with their lower efficacy in stabilizing an active conformation of extracellular domain (Figure 4) and likely account for their partial agonism (Figures 2B–2D).

Nb9-8 stabilizes the high-affinity state for agonists by binding to the cytoplasmic surface of the receptor. Interestingly, we observed agonist-specific chemical shift changes for M202$^{5.54}$ and M143$^{4.45}$ in M2R bound to Nb9-8 (Figures 6E and 6F). The ε-methyls of M202$^{5.54}$ and M143$^{4.45}$ are located about 11 and 19 Å apart from Nb9-8, respectively; therefore the surrounding chemical environments should not be affected directly by Nb9-8 itself (Figure 6B). The addition of Nb9-8 causes a further upfield shift of the M202$^{5.54}$ peak for M2R bound to iperoxo or PR15, probably as a result of the formation of fully active conformation of TMs 5, 6, and 7 (Figure 6A). Interestingly, we observed a similar upfield shift in M2R bound to pilocarpine; however, the peak looks more irregular and has much weaker intensity (Figure 6F; Figure S6D). When M2R binds to ACh and Nb9-8 or carbachol and Nb9-8, the M202$^{5.54}$ peak shifts to a completely different position than observed for iperoxo, PR15, or pilocarpine and Nb9-8 (Figure 6E). The distinct chemical shift for M202$^{5.54}$ indicates that ACh and carbachol stabilize a distinct active conformation of TM5 from that observed in the active structure of M2R bound to iperoxo and Nb9-8.

The spectral changes of M143$^{4.45}$ upon Nb9-8 binding may result from its interaction with ICL2 and TM3 (Figure 6B). Although peak intensities of M202$^{5.54}$ are enhanced to some extent by the addition of Nb9-8 to M2R bound to full or super-agonists (Figure S5D), the M143$^{4.45}$ signal is more heterogeneous with lower peak intensities when Nb9-8 is added to M2R bound to agonists (Figures 6F and S5E). These results show that Nb9-8 does not stabilize the receptor in uniform active conformation, particularly the intracellular conformation, and that the ligand-specific differences that we observe in the presence of Nb9-8 likely contribute to their distinct signaling behaviors.

Structural and Dynamical Insights into the Supraphysiological Signaling Efficacies

In an effort to understand how the differences in chemical structure could stabilize different receptor conformations having different signaling behavior, especially the super-efficacy of iperoxo and PR15 (Figures 2C–2E), we performed MD simulations of

the M2R-Nb9-8 complex bound to iperoxo, PR15, ACh, and carbachol (Figure S7A). All simulations were initiated from the crystal structure coordinates. We first looked for differences between the binding poses of the super-agonists iperoxo and PR15 and the full agonists ACh and carbachol. Figure 7A shows a superposition of the binding poses of the four agonists. As a result of their acetylene spacer unit, iperoxo and PR15 bind deeper into the receptor core than ACh and carbachol, while the ammonium head adopts a similar pose. This deeper binding pose, observed only for iperoxo and PR15, enables a direct interaction with W400$^{6.48}$, resulting in a rotation of the W400$^{6.48}$ side chain, observed in the crystal structure of the M2R in complex with iperoxo and Nb9-8 (Kruse et al., 2013). In contrast, ACh and carbachol do not bind as deep in the receptor core and would not be as effective at stabilizing the rotamer of W400$^{6.48}$ (Figure 7B). As shown in Figure 7C, the side chain of W400$^{6.48}$ remains stable in simulations of the M2R bound to iperoxo and PR15, while in simulations of the M2R bound to ACh and carbachol, W400$^{6.48}$ transitions between two rotameric states. These differences are likely to explain some of the differences observed in the spectrum of M202$^{5.54}$ (Figures 6C and 6E), which would be influenced by the ring currents from W400$^{6.48}$ through F396$^{6.44}$ (Figure 6A). W$^{6.48}$ is highly conserved among family A GPCRs and has been proposed to play a role in agonist stabilized conformational changes in TM6 (Kobilka and Deupi, 2007; Shi et al., 2002).

As noted above, PR15 stabilizes a receptor conformation that is similar to iperoxo. Although the spectrum of carbachol bound M2R is similar to that of ACh, in both absence and presence of Nb9-8, there are substantial differences between the two classes of agonists. This can best be seen by comparing the full HSQC spectra of the four agonists (Figures S7B–S7D). Thus, MD simulations and NMR spectra provide a plausible mechanism accounting for the supraphysiological efficacy of G-protein signaling for iperoxo and PR15. Moreover, although PR15 was able to stabilize a small fraction of the receptor in the same active-state conformation as iperoxo, it was nearly as effective as iperoxo at stabilizing the TM5-TM6 interface in a fully active conformation in the presence of Nb9-8 (Figure S7C). This can best be explained by MD simulations showing that PR15 and iperoxo are more effective at stabilizing the active rotamer of the "toggle switch" W400$^{6.48}$ (Figures 7B and 7C). These observations suggest that the ability to stabilize even a small fraction of the M2R in the same active conformation as that stabilized by iperoxo is sufficient for maximal G protein activation, most likely because microsecond to millisecond dynamics maintain a constant pool of M2R in the active state available for G protein coupling.

As noted above, only iperoxo exhibits super-efficacy in the arrestin signaling pathway (Figure 2B), a property that may be explained by the iperoxo-specific receptor ligand interactions. The previously determined crystal structure of M2R revealed a direct hydrogen bond between the endocyclic oxygen of iperoxo and the nitrogen of N404$^{6.52}$ (Kruse et al., 2013). Our simulations suggest that this interaction is unique for iperoxo, and there might be an additional water-mediated interaction between endocyclic nitrogen of iperoxo and the oxygen of N404$^{6.52}$, while all other ligands investigated are able to form only a water-mediated interaction to N404$^{6.52}$, despite starting from a docking pose enabling
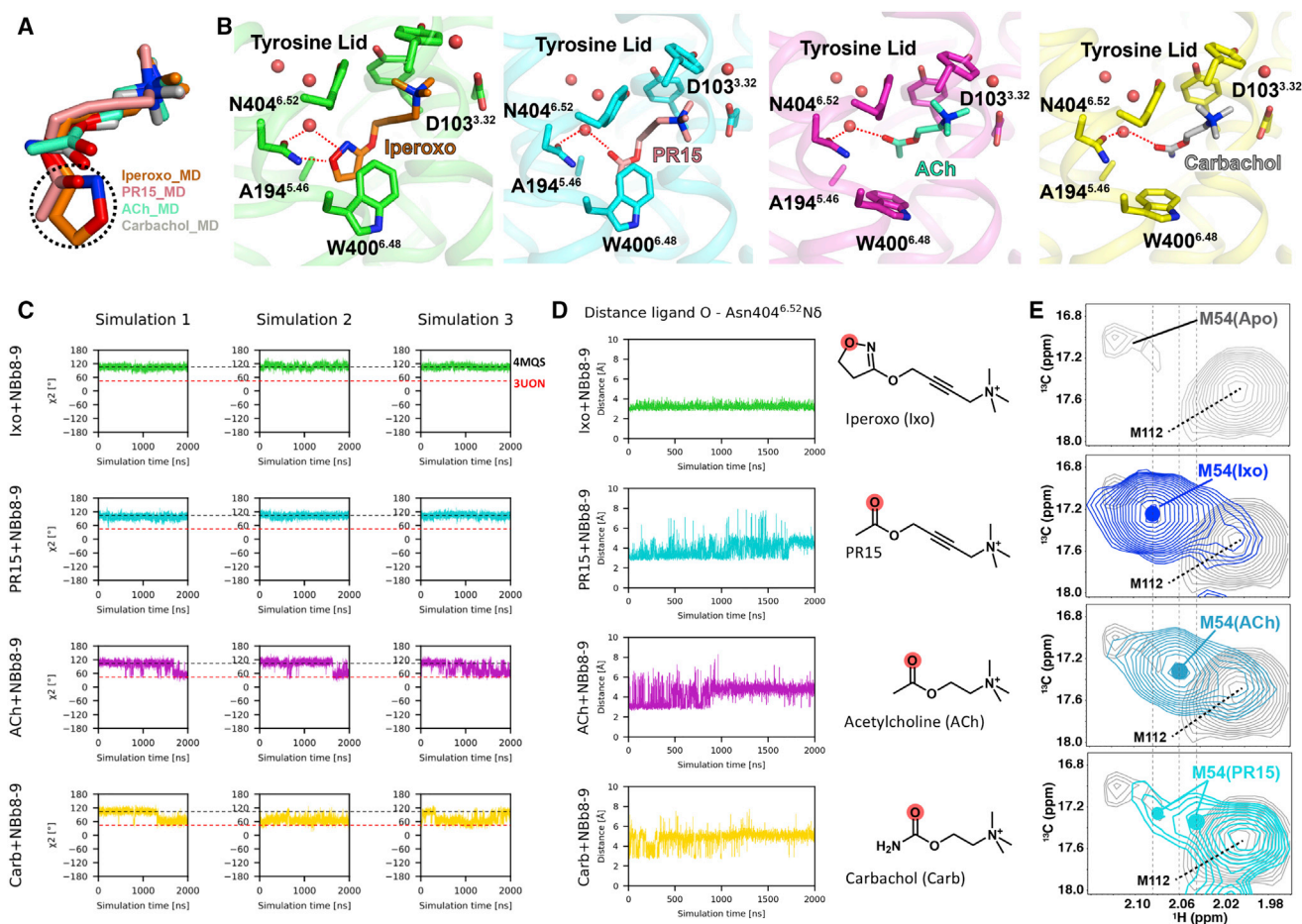
Figure 7. MD Simulations and Agonist-Dependent Conformational States of M54

(A) Superposition of iperoxo, PR15, ACh, and carbachol from MD simulations. The longer structures of iperoxo and PR15 bind deeper into the receptor core, highlighted by the dashed circle.

(B) Comparison of binding modes from MD simulations of iperoxo, PR15, ACh, and carbachol. Red spheres represent water molecules. The direct H-bond and water-mediated interactions between agonists and N404[6.52] are shown as red dashed lines.

(C) MD simulations show a ligand-dependent rotamer of W[6.48] consistent over multiple simulations. The dashed black and red lines indicate the dihedral angle of W[6.48] in the active (PDB: 4MQS, 109°) and inactive (PDB: 3UON, 52°) crystal structures, respectively.

(D) Simulation traces of the distance between the oxygen in each ligand (highlighted in red) and the δN of N404[6.52]. We observed a stable direct H bond with the δN of N404[6.52] only in the case of iperoxo.

(E) Agonist-specific spectral changes of M54 in ICL1. The data of M54 were processed with a sine-bell window function and an additional Lorentz-to-Gauss window function in 1H dimension.

See also Figure S7.

a direct interaction (Figures 7B and 7D). Furthermore, compared with PR15, the bulkier isoxazole ring of iperoxo has a larger interaction surface with W400[6.48] and additionally interacts with A194[5.46], which could result in a more stable active conformation of TMs 3, 5, and 6 than produced by the smaller acetyl group of PR15 (Figure 7B). This is consistent with the much stronger signal observed in M202[5.54] for iperoxo relative to PR15 (Figures 6C and S5D). Thus, we suggest that the hydrogen bond between iperoxo and the nitrogen of N404[6.52] and its larger interaction surface toward W400[6.48] are important for the supraphysiological efficacy observed in the arrestin signaling pathway.

Recent structures of the rhodopsin-arrestin (Kang et al., 2015) and rhodopsin-G$_i$ (Kang et al., 2018) complexes reveal that ICL1

and H8 of rhodopsin are involved in the interaction with arrestin but not G$_i$ (Figure S7E). We then investigated ligand-stabilized conformational changes at the ICL1-H8 interface by introducing a L54M mutation (Figures S7F and S7G). The ε-methyl of L54M would be expected to lie in the space between ICL1 and H8. In the absence of an agonist the signal from L54M is very weak. This is likely due to immobilization of the L54M side chain by packing interactions with H8, as suggested by the inactive-state structure of the M2R (Figure S7F). Binding of iperoxo and ACh leads to an upfield shift and a marked increase in the L54M intensity (Figures 7E and S7H). Structural changes associated with agonist binding, the outward movement of TM6 and the inward movement of TM7 and H8 (Figure S7F), would be expected to

CellPress

alter interactions between L54M and H8. We observed that the iperoxo stabilized L54M peak is quite different from that of PR15 in both chemical shift and peak intensity. Although ACh also stabilized a strong peak for M54, the chemical shift is distinct from that of iperoxo (Figures 7E and S7H). It is notable that a number of family A GPCR-G protein complex structures show little interaction between ICL1 or H8 and the G-protein (Draper-Joyce et al., 2018; García-Nafría et al., 2018; Koehl et al., 2018), hence, the conformational changes at the ICL1-H8 interface may be more important for arrestin binding. These results suggest that iperoxo stabilizes a different orientation of ICL1 and H8 relative to that stabilized by ACh and PR15. These distinct structural and dynamical features of iperoxo-bound M2R may account for its unique supraphysiological efficacy in arrestin signaling pathway.

DISCUSSION

Taking advantage of solution NMR, we investigated the conformational complexity and dynamics of the M2R by monitoring the chemical environments of $^{13}CH_3$-ε-methionines in the extracellular vestibule, TM core, and G protein coupling domain. The chemical shift fingerprints of $^{13}CH_3$-ε-methionines in these domains, particularly for M202$^{5.54}$ in TM5, revealed a number of conformational states not observed by crystallography. In combination with functional analysis and MD simulations, our studies provide potential structural and dynamical insights into the super-efficacies of iperoxo toward G protein and β-arrestin signaling pathways.

In the previous $^{13}CH_3$-ε-methionine NMR studies of β2AR (Kofuku et al., 2012), the chemical shifts for different ligands correlated well with their efficacies, which suggests a conformational equilibrium between the inverse agonist-bound and full agonist-bound states. This phenomenon was also found in the recent NMR studies of the turkey β1AR (Solt et al., 2017), in which nearly all probes showed chemical shift changes that had a linear correlation with ligand efficacy. NMR studies of μOR (Okude et al., 2015) using the same labeling strategy also showed a strong linear correlation between signaling bias and chemical shift for different agonists. In contrast in the M2R, we did not observe a strong linear correlation between ligand efficacy or signaling bias and the chemical shift. The only exception is M77$^{2.58}$ in the extracellular vestibule (Figure 4D). Instead, our results suggest that each ligand stabilizes a distinct conformation or set of conformations. They also suggest that the M2R may be more dynamic and conformationally complex than the β2AR, the turkey β1AR, or the μOR. As noted above, a unique feature of M2R among these other receptors is found in the core of the receptor where I$^{3.40}$, P$^{5.50}$, and F$^{6.44}$ pack tightly together with different side chain arrangements in the active and inactive states of the β2AR and the μOR (Figure 5A). In contrast, in the M2R, the smaller side chain of V$^{3.40}$ has weaker interactions with P$^{5.50}$ and F$^{6.44}$ (Figure 5A) and would not be expected to stabilize distinct active and inactive states.

In conclusion, our studies reveal that the M2R may be more conformationally complex than other GPCRs that have been studied using NMR spectroscopy. MD simulations provide additional insights into the mechanism by which ligands stabilize specific receptor conformations that are correlated with different efficacy profiles. A better understanding of the relationships between ligand structures and the receptor conformations they stabilize may facilitate the development of drugs that are capable of regulating specific signaling pathways.

STAR★METHODS

Detailed methods are provided in the online version of this paper and include the following:

- KEY RESOURCES TABLE
- CONTACT FOR REAGENT AND RESOURCE SHARING
- EXPERIMENTAL MODEL AND SUBJECT DETAILS
- METHOD DETAILS
  - Preparation of $^{13}CH_3$-ε-methionines labeled M2R
  - Expression and purification of Nb9-8
  - Expression and purification of heterotrimeric GoA
  - GTPase-Glo^{TM} assay
  - NMR spectroscopy
  - Radio-ligand binding assay
  - Molecular dynamics simulations
  - G-protein IP-1 assay and β-arrestin recruitment assay
  - Calculation of signaling bias
  - General materials and methods of organic synthesis
  - Synthetic procedures for PR15

SUPPLEMENTAL INFORMATION

Supplemental Information can be found online at https://doi.org/10.1016/j.molcel.2019.04.028.

AUTHOR CONTRIBUTIONS

J.X. designed NMR experiments, performed the radioligand binding assays and protein purifications, and collected and analyzed NMR data. Y.H. conducted the NMR experiments and assisted with NMR data processing and analysis. X.N. and H.L. assisted with NMR data collection. H.H. performed the G protein IP-1 assay and β-arrestin recruitment assay. P.R. synthesized PR15. J.K. performed the MD simulations experiments and analyzed the data. S.M. and J.X. performed the GTPase Glo assay. P.G. supervised G protein IP-1 and β-arrestin recruitment assays, PR15 synthesis, and MD simulations. C.J. supervised all NMR experiments and data processing. B.K.K. provided overall project supervision. J.X. and B.K.K. wrote the manuscript with contributions from all authors.

DECLARATION OF INTERESTS

B.K.K. is a co-founder of and consultant for ConfometRx, Inc.

CellPress

REFERENCES

Abraham, M.J., Murtola, T., Schulz, R., Páll, S., Smith, J.C., Hess, B., and Lindahl, E. (2015). GROMACS: high performance molecular simulations through multi-level parallelism from laptops to supercomputers. SoftwareX *1-2*, 19–25.

Bayly, C.I., Cieplak, P., Cornell, W.D., and Kollman, P.A. (1993). A well-behaved electrostatic potential based method using charge restraints for deriving atomic charges—the Resp model. J. Phys. Chem. *97*, 10269–10280.

Bebbington, A., Brimblecombe, R.W., and Shakeshaft, D. (1966). The central and peripheral activity of acetylenic amines related to oxotremorine. Br. J. Pharmacol. Chemother. *26*, 56–67.

Carpenter, B., Nehmé, R., Warne, T., Leslie, A.G.W., and Tate, C.G. (2016). Erratum: structure of the adenosine A_{2A} receptor bound to an engineered G protein. Nature *538*, 542.

Case, D.A., Ben-Shalom, I.Y., Brozell, S.R., Cerutti, D.S., Cheatham, I.T.E., Cruzeiro, V.W.D., Darden, T.A., Duke, R.E., Ghoreishi, D., Gilson, M.K., et al. (2018). Amber 2018 Reference Manual (University of California, San Francisco). http://ambermd.org/doc12/Amber18.pdf.

Conn, P.J., Jones, C.K., and Lindsley, C.W. (2009). Subtype-selective allosteric modulators of muscarinic receptors for the treatment of CNS disorders. Trends Pharmacol. Sci. *30*, 148–155.

Darden, T., York, D., and Pedersen, L. (1993). Particle mesh Ewald: an N·log(N) method for Ewald sums in large systems. J. Chem. Phys. *98*, 10089–10092.

Delaglio, F., Grzesiek, S., Vuister, G.W., Zhu, G., Pfeifer, J., and Bax, A. (1995). NMRPipe: a multidimensional spectral processing system based on UNIX pipes. J. Biomol. NMR *6*, 277–293.

Dickson, C.J., Madej, B.D., Skjevik, A.A., Betz, R.M., Teigen, K., Gould, I.R., and Walker, R.C. (2014). Lipid14: the amber lipid force field. J. Chem. Theory Comput. *10*, 865–879.

Draper-Joyce, C.J., Khoshouei, M., Thal, D.M., Liang, Y.L., Nguyen, A.T.N., Furness, S.G.B., Venugopal, H., Baltos, J.A., Plitzko, J.M., Danev, R., et al. (2018). Structure of the adenosine-bound human adenosine A_1 receptor-G_i complex. Nature *558*, 559–563.

Dror, R.O., Arlow, D.H., Maragakis, P., Mildorf, T.J., Pan, A.C., Xu, H., Borhani, D.W., and Shaw, D.E. (2011). Activation mechanism of the β2-adrenergic receptor. Proc. Natl. Acad. Sci. U S A *108*, 18684–18689.

Dror, R.O., Green, H.F., Valant, C., Borhani, D.W., Valcourt, J.R., Pan, A.C., Arlow, D.H., Canals, M., Lane, J.R., Rahmani, R., et al. (2013). Structural basis for modulation of a G-protein-coupled receptor by allosteric drugs. Nature *503*, 295–299.

Frisch, M.J., Trucks, G.W., Schlegel, H.B., Scuseria, G.E., Robb, M.A., Cheeseman, J.R., Scalmani, G., Barone, V., Mennucci, B., Petersson, G.A., et al. (2010). Gaussian 09, Revision B.01 (Gaussian).

García-Nafría, J., Nehmé, R., Edwards, P.C., and Tate, C.G. (2018). Cryo-EM structure of the serotonin 5-HT$_{1B}$ receptor coupled to heterotrimeric G$_o$. Nature *558*, 620–623.

Gregory, K.J., Sexton, P.M., and Christopoulos, A. (2007). Allosteric modulation of muscarinic acetylcholine receptors. Curr. Neuropharmacol. *5*, 157–167.

Haga, K., Kruse, A.C., Asada, H., Yurugi-Kobayashi, T., Shiroishi, M., Zhang, C., Weis, W.I., Okada, T., Kobilka, B.K., Haga, T., and Kobayashi, T. (2012). Structure of the human M2 muscarinic acetylcholine receptor bound to an antagonist. Nature *482*, 547–551.

Huang, W., Manglik, A., Venkatakrishnan, A.J., Laeremans, T., Feinberg, E.N., Sanborn, A.L., Kato, H.E., Livingston, K.E., Thorsen, T.S., Kling, R.C., et al. (2015). Structural insights into μ-opioid receptor activation. Nature *524*, 315–321.

Hunter, J.D. (2007). Matplotlib: a 2D graphics environment. Comput. Sci. Eng. *9*, 90–95.

Johnson, B.A., and Blevins, R.A. (1994). NMR View: a computer program for the visualization and analysis of NMR data. J. Biomol. NMR *4*, 603–614.

Jones, E.R.H., Marszak, I., and Bader, H. (1947). The Mannich reaction with monosubstituted acetylenic compounds. J. Chem. Soc. 1578–1579.

Kang, Y., Zhou, X.E., Gao, X., He, Y., Liu, W., Ishchenko, A., Barty, A., White, T.A., Yefanov, O., Han, G.W., et al. (2015). Crystal structure of rhodopsin bound to arrestin by femtosecond x-ray laser. Nature *523*, 561–567.

Kang, Y., Kuybeda, O., de Waal, P.W., Mukherjee, S., Van Eps, N., Dutka, P., Zhou, X.E., Bartesaghi, A., Erramilli, S., Morizumi, T., et al. (2018). Cryo-EM structure of human rhodopsin bound to an inhibitory G protein. Nature *558*, 553–558.

Kenakin, T., Watson, C., Muniz-Medina, V., Christopoulos, A., and Novick, S. (2012). A simple method for quantifying functional selectivity and agonist bias. ACS Chem. Neurosci. *3*, 193–203.

Kloeckner, J., Schmitz, J., and Holzgrabe, U. (2010). Convergent, short synthesis of the muscarinic superagonist iperoxo. Tetrahedron Lett. *51*, 3470–3472.

Kobilka, B.K., and Deupi, X. (2007). Conformational complexity of G-protein-coupled receptors. Trends Pharmacol. Sci. *28*, 397–406.

Koehl, A., Hu, H., Maeda, S., Zhang, Y., Qu, Q., Paggi, J.M., Latorraca, N.R., Hilger, D., Dawson, R., Matile, H., et al. (2018). Structure of the μ-opioid receptor-G$_i$ protein complex. Nature *558*, 547–552.

Kofuku, Y., Ueda, T., Okude, J., Shiraishi, Y., Kondo, K., Maeda, M., Tsujishita, H., and Shimada, I. (2012). Efficacy of the β$_2$-adrenergic receptor is determined by conformational equilibrium in the transmembrane region. Nat. Commun. *3*, 1045.

Kruse, A.C., Ring, A.M., Manglik, A., Hu, J., Hu, K., Eitel, K., Hübner, H., Pardon, E., Valant, C., Sexton, P.M., et al. (2013). Activation and allosteric modulation of a muscarinic acetylcholine receptor. Nature *504*, 101–106.

Langmead, C.J., and Christopoulos, A. (2013). Supra-physiological efficacy at GPCRs: superstition or super agonists? Br. J. Pharmacol. *169*, 353–356.

Lans, I., Dalton, J.A.R., and Giraldo, J. (2015). Helix 3 acts as a conformational hinge in Class A GPCR activation: An analysis of interhelical interaction energies in crystal structures. J. Struct. Biol. *192*, 545–553.

Liu, H., Kim, H.R., Deepak, R.N.V.K., Wang, L., Chung, K.Y., Fan, H., Wei, Z., and Zhang, C. (2018). Orthosteric and allosteric action of the C5a receptor antagonists. Nat. Struct. Mol. Biol. *25*, 472–481.

Lomize, M.A., Lomize, A.L., Pogozheva, I.D., and Mosberg, H.I. (2006). OPM: Orientations of Proteins in Membranes Database. Bioinformatics *22*, 623–625.

Maier, J.A., Martinez, C., Kasavajhala, K., Wickstrom, L., Hauser, K.E., and Simmerling, C. (2015). ff14SB: improving the accuracy of protein side chain and backbone parameters from ff99SB. J. Chem. Theory Comput. *11*, 3696–3713.

Mittermaier, A.K., and Kay, L.E. (2009). Observing biological dynamics at atomic resolution using NMR. Trends Biochem. Sci. *34*, 601–611.

Mojtahedi, M.M., and Samadian, S. (2013). Efficient and rapid solvent-free acetylation of alcohols, phenols, and thiols using catalytic amounts of sodium acetate trihydrate. J. Chem. *2013*, 1–7.

Namkung, Y., Radresa, O., Armando, S., Devost, D., Beautrait, A., Le Gouill, C., and Laporte, S.A. (2016). Quantifying biased signaling in GPCRs using BRET-based biosensors. Methods *92*, 5–10.

Nygaard, R., Zou, Y., Dror, R.O., Mildorf, T.J., Arlow, D.H., Manglik, A., Pan, A.C., Liu, C.W., Fung, J.J., Bokoch, M.P., et al. (2013). The dynamic process of β(2)-adrenergic receptor activation. Cell *152*, 532–542.

Okude, J., Ueda, T., Kofuku, Y., Sato, M., Nobuyama, N., Kondo, K., Shiraishi, Y., Mizumura, T., Onishi, K., Natsume, M., et al. (2015). Identification of a conformational equilibrium that determines the efficacy and functional selectivity of the μ-opioid receptor. Angew. Chem. Int. Ed. Engl. *54*, 15771–15776.

Pettersen, E.F., Goddard, T.D., Huang, C.C., Couch, G.S., Greenblatt, D.M., Meng, E.C., and Ferrin, T.E. (2004). UCSF Chimera—a visualization system for exploratory research and analysis. J. Comput. Chem. *25*, 1605–1612.

Rasmussen, S.G., DeVree, B.T., Zou, Y., Kruse, A.C., Chung, K.Y., Kobilka, T.S., Thian, F.S., Chae, P.S., Pardon, E., Calinski, D., et al. (2011). Crystal structure of the β2 adrenergic receptor-Gs protein complex. Nature *477*, 549–555.

Roe, D.R., and Cheatham, T.E., 3rd (2013). PTRAJ and CPPTRAJ: software for processing and analysis of molecular dynamics trajectory data. J. Chem. Theory Comput. *9*, 3084–3095.

Shi, L., Liapakis, G., Xu, R., Guarnieri, F., Ballesteros, J.A., and Javitch, J.A. (2002). Beta2 adrenergic receptor activation. Modulation of the proline kink in transmembrane 6 by a rotamer toggle switch. J. Biol. Chem. *277*, 40989–40996.

Solt, A.S., Bostock, M.J., Shrestha, B., Kumar, P., Warne, T., Tate, C.G., and Nietlispach, D. (2017). Insight into partial agonism by observing multiple equilibria for ligand-bound and G_s-mimetic nanobody-bound $β_1$-adrenergic receptor. Nat. Commun. *8*, 1795.

Sounier, R., Mas, C., Steyaert, J., Laeremans, T., Manglik, A., Huang, W., Kobilka, B.K., Déméné, H., and Granier, S. (2015). Propagation of conformational changes during μ-opioid receptor activation. Nature *524*, 375–378.

Van Der Spoel, D., Lindahl, E., Hess, B., Groenhof, G., Mark, A.E., and Berendsen, H.J. (2005). GROMACS: fast, flexible, and free. J. Comput. Chem. *26*, 1701–1718.

van der Westhuizen, E.T., Breton, B., Christopoulos, A., and Bouvier, M. (2014). Quantification of ligand bias for clinically relevant β2-adrenergic receptor ligands: implications for drug taxonomy. Mol. Pharmacol. *85*, 492–509.

van Koppen, C.J., and Kaiser, B. (2003). Regulation of muscarinic acetylcholine receptor signaling. Pharmacol. Ther. *98*, 197–220.

Wess, J., Eglen, R.M., and Gautam, D. (2007). Muscarinic acetylcholine receptors: mutant mice provide new insights for drug development. Nat. Rev. Drug Discov. *6*, 721–733.

Wishart, D.S. (2011). Interpreting protein chemical shift data. Prog. Nucl. Magn. Reson. Spectrosc. *58*, 62–87.

Wolf, M.G., Hoefling, M., Aponte-Santamaría, C., Grubmüller, H., and Groenhof, G. (2010). g_membed: Efficient insertion of a membrane protein into an equilibrated lipid bilayer with minimal perturbation. J. Comput. Chem. *31*, 2169–2174.

Ye, L., Van Eps, N., Zimmer, M., Ernst, O.P., and Prosser, R.S. (2016). Activation of the A2A adenosine G-protein-coupled receptor by conformational selection. Nature *533*, 265–268.

CellPress

STAR★METHODS

KEY RESOURCES TABLE

REAGENT or RESOURCE	SOURCE	IDENTIFIER
Bacterial and Virus Strains		
E. coli cells BL21(DE3)	CWBIO	CW0809S
E. coli cells TOP10	CWBIO	CW0807S
E. coli cells DH10Bac	Invitrogen	10361012
Chemicals, Peptides, and Recombinant Proteins		
Benzamidine	Sigma	Cat#B6506
Leupeptin	Sigma	Cat#L2884
n-dodecyl-beta-D-maltopyranoside (DDM)	Anatrace	Cat#D310
Lauryl Maltose Neopentyl Glycol (MNG)	Anatrace	Cat#NG310
Cholesterol hemisucinate (CHS)	Sigma	Cat#C6512
Sodium Cholate hydrate	Sigma	Cat#C1254
Iodoacetamide	Sigma	Cat#I6125
ANTI-FLAG M1 Agarose Affinity Gel	Sigma-Aldrich	Cat#A4596
FLAG peptide	Sigma-Aldrich	Cat# F3290
Atropine sulfate salt monohydrate	Sigma	Cat#A0257
Iperoxo	Sigma	Cat#SML0790
Acetylcholine	Sigma	Cat#A5626
Pilocarpine	Selleck	Cat#S4231
Xanomeline	Sigma	Cat#X2754
Tiotropium	abcam	Cat#ab143219
QNB	TRC	Cat#Q795800
Scopolamine	Selleck	Cat#S2508
Gallamine	Selleck	Cat#S2471
Carbachol	abcam	Cat#ab141354
PR15	This study / own lab synthesis	N/A
[^{3}H]-NMS	PerkinElmer	Cat#NET636001MC
ESF921 culture medium	Expression Systems	Cat# 96-001
ESF921 culture medium, Methionine Deficient	Expression Systems	Cat# 96-200
L-METHIONINE (METHYL-^{13}C,99%)	Cambridge Isotope Laboratories	Cat#CLM-206-0
DEUTERIUM OXIDE (D$_2$O)	Cambridge Isotope Laboratories	Cat#DLM-4-1000
2,2-dimethyl-2-silapentane-5-sulfonic acid (DSS)	Cambridge Isotope Laboratories	Cat#DLM-32-10
Dimethyl sulfoxide-d$_6$	Sigma	Cat#151874
Lambda Protein Phosphatase (Lambda PP)	New England Biolabs	Cat# P0753
TCEP	Sigma-Aldrich	Cat# C4706
Antarctic Phosphatase	New England Biolabs	Cat# M0289
CIP	New England Biolabs	Cat# M0290
DpnI	New England Biolabs	Cat# R0176
Critical Commercial Assays		
GTPase-Glo^{TM} kit	Promega	Cat#V7681
FuGENE HD Transfection Reagent	Promega	Cat#E2311
Arrestin recruitment assay	DiscoverX, now Eurofins	Cat#93-0001
IP-One assay	CisBio	Cat#62IPAPEC
Experimental Models: Cell Lines		
Insect cell line Sf9	Expression Systems	N/A
Insect cell line High Fives (Tni)	Expression Systems	N/A

Continued

REAGENT or RESOURCE	SOURCE	IDENTIFIER
Recombinant DNA		
pfastbac-wtM2R	This study	N/A
pfastbac-mutM2R	This study	N/A
pfastbac-Gαo	This study	N/A
pfastbac-dual-Gβ/Gγ	This study	N/A
pMal-p2x-Nb9-8	This study	N/A
Software and Algorithms		
PyMOL	Schrödinger	https://www.pymol.org/2/
Prism v.6.0	GraphPad Software	https://www.graphpad.com/scientific-software/prism/
NMRpipe	Delaglio et al., 1995	https://www.ibbr.umd.edu/nmrpipe/index.html
NMRViewJ	Johnson and Blevins, 1994	http://www.onemoonscientific.com
GOLD Suite v5.4	CCDC	https://www.ccdc.cam.ac.uk/
GROMACS v.2018.1	Van Der Spoel et al., 2005	http://www.gromacs.org/
CPPTRAJ, AmberTools18	Case et al., 2018	http://ambermd.org/index.php
UCSF Chimera v.1.12	Pettersen et al., 2004	https://www.cgl.ucsf.edu/chimera/
Matplotlib v.2.2.2	Hunter, 2007	https://matplotlib.org/

CONTACT FOR REAGENT AND RESOURCE SHARING

Further information and requests for reagents should be directed to and will be fulfilled by the Lead Contact, Brian. K. Kobilka (kobilka@stanford.edu).

EXPERIMENTAL MODEL AND SUBJECT DETAILS

Human M2R was expressed in Sf9 cells infected with recombinant baculovirus (pFastBac, Invitrogen). Human Gα and Gβγ were expressed in HighFive insect cells.

METHOD DETAILS

Preparation of $^{13}CH_3$-ε-methionines labeled M2R

The construct referred to as M2Rmini was derived from the sequence that used in previously crystallographic studies by adding back four glycosylation sites at the N terminus. Combinatorial Met→Leu or Met→Thr mutations (Figures S2–S4) were introduced into the M2Rmini construct for NMR resonance assignments. The construct referred to as M2Rmini$_\Delta$5M was made by introducing five methionine mutations (M01, M45, M139, M142, M456) into the M2Rmini construct. The construct referred to as M2RFL_miniMet was made by introducing 6 methionine mutations in the transmembrane bundle (M01, M45, M139, M142, M143, M456) and 3 methionine mutations in the ICL3 (M248, M296, M368). Recombinant baculovirus for insect cell expression was made using the Bac-to-Bac system (Invitrogen). The receptor was expressed in baculovirus-infected insect cells as previously described (Kruse et al., 2013) with slight modification to achieve the selective labeling of $^{13}CH_3$-ε-methionines. Specifically, Sf9 cells were grown in the methionine deficient media (Expression system) and infected at a density of 4×10^6 cells ml^{-1} in the presence of 10 μM atropine. At the same time, $^{13}CH_3$-ε-methionine (Cambridge Isotope Laboratory, dissolved in sterile deionized H_2O) was added into the media at 250 mg L^{-1} concentration and then incubated for two days at 27°C. The unlabeled M2R was expressed in the same way in normal insect cell media (Expression system) without adding $^{13}CH_3$-ε-methionine. After incubation, the cells were spun down and pellets were stored at −80°C until use.

Cell pellets were resuspended in a lysis buffer (10 mM Tris, 1 mM EDTA, 10 μM atropine, 2.5 μg ml^{-1} leupeptin, 160 μg ml^{-1} benzamidine) to lyse the cells by hypotonic. Cell membranes were then spun down and solubilized with a buffer of 20 mM HEPEs pH 7.5, 750 mM NaCl, 1% dodecyl maltoside (DDM, Anatrace), 0.2% Sodium Cholate, 0.03% cholesterol hemisuccinate (CHS, Sigma), 10 μM atropine, 2.5 μg ml^{-1} leupeptin, 160 μg ml^{-1} benzamidine, 1 mg ml^{-1} iodoacetamide, and 30% glycerol. Nickel-NTA Sepharose (GE Healthcare) was then added into the solubilized receptor and rotated for 2 h at 4°C. The resin was then spun down and washed in batch for three times with a buffer containing 20 mM HEPEs pH 7.5, 750 mM NaCl, 0.1% DDM, 0.02% sodium cholate, 0.03% CHS, 10 μM atropine, 2.5 μg ml^{-1} leupeptin, 160 μg ml^{-1} benzamidine, and 30% glycerol. The washed resin was poured into a glass column and receptor was eluted in the wash buffer supplemented with 250 mM imidazole.

The Ni-NTA chromatography purified receptor was then loaded onto a column with anti-flag M1 affinity resin and was extensively washed with a buffer containing 20 mM HEPEs pH 7.5, 100 mM NaCl, 0.1% DDM, 0.02% sodium cholate, 0.003% CHS and supplemented with 2 mM $CaCl_2$ (For preparation of the apo-state receptor, no ligand was added into all the subsequent buffers). The receptor was then gradually exchanged into a buffer containing 20 mM HEPEs pH 7.5, 100 mM NaCl, 0.01% lauryl maltose neopentyl glycol (LMNG, Anatrace), 0.003% CHS supplemented with 2 mM $CaCl_2$, and then eluted with same buffer supplemented with 0.2 mg ml^{-1} flag peptide and 5 mM EDTA. The flag affinity chromatography purified receptor was concentrated to 500 μL and finally purified by SEC chromatography with a buffer containing 20 mM HEPEs pH 7.5, 100 mM NaCl, 0.01% LMNG, 0.003% CHS prepared in D_2O (> 99%). The monodisperse peak fractions was collected and then concentrated to a final concentration of around 100 μM using a 50 kDa molecular weight cutoff Millipore concentrator.

The ligands used in our NMR studies were dissolved in perdeuterated dimethyl d6-sulfoxide to a stock concentration of 100 mM and were added to the sample in the Shigemi microtube (Shigemi Inc.) at a saturating concentration (around 1 mM). Nb9-8 was added directly to the agonist bound sample at a final concentration of 120-150 μM and incubated at room temperature for at least 30 minutes before data acquisition. Samples before NMR or after NMR were analyzed by SEC chromatography and SDS-PAGE to make sure the receptor was functional during the NMR experiments (Figures S1I and S1J).

Expression and purification of Nb9-8

The nanobody Nb9-8 was expressed and purified as previously described (Kruse et al., 2013). Briefly, pMalp2x-Nb9-8 plasmids were transformed into *E. coli* BL21(DE3) cells. Cells were grown to A_{600} = 0.8 at 37°C in TB media containing 0.1% glucose, 2 mM $MgCl_2$ and 50 μg ml^{-1} ampicillin. Cells were then induced by addition of 1 mM IPTG and were incubated overnight at 22°C. Cells were harvest and periplasmic protein was obtained by osmotic shock. MBP-Nb9-8 fusion proteins were purified by Ni-NTA chromatography and MBP was removed using 3C protease. Cleaved MBP was separated from the nanobodies by an additional Ni-NTA purification step. The Ni-NTA chromatography purified nanobodies were then purified by SEC chromatography with a buffer containing 20 mM HEPEs pH 7.5, 100 mM NaCl. The purified nanobodies were exchanged to the same buffer prepared in D_2O by repeated dilution and concentration using a 3 kDa molecular weight cutoff Millipore concentrator, and were finally concentrated to a concentration at around 1.5 mM. The concentrated nanobodies were aliquoted, flash frozen in liquid nitrogen and frozen at −80°C before use.

Expression and purification of heterotrimeric GoA

Human Gαo and Gβ1γ2 with 3C protease-cleavable 6xHis-tag were expressed in HighFive insect cells grown in ESF921 cell medium. Cultures were grown to a density of 3 million cells per ml and then infected with Gαo and G β1γ2 baculovirus at a ratio of 10-20 mL L^{-1} and 1-2 mL L^{-1} respectively. After 48 h of incubation the infected cells were harvested by centrifugation and stored at −80°C until use.

Cell pellets were resuspended in 75 mL lysis buffer (10 mM Tris, pH 7.5, 0.1 mM $MgCl_2$, 5 mM β-mercaptoethanol (β-ME), 10 μM GDP, 2.5 μg ml^{-1} leupeptin and 160 μg ml^{-1} benzamidine) per liter of culture volume and were stirred at RT for 15 minutes. Cell membranes were then spun down and resuspended with 100 mL solubilization buffer (20 mM HEPES, pH 7.5, 100 mM NaCl, 1% Sodium Cholate, 0.05% DDM, 5 mM $MgCl_2$, 2 μL CIP, 5 mM β-ME, 15 mM imidazole, 10 μM GDP, 2.5 μg ml^{-1} leupeptin and 160 μg ml^{-1} benzamidine) per liter of culture volume using a Dounce homogenizer. The sample were stirred at 4°C for 40 minutes, and then centrifuged for 30 minutes to remove insoluble debris.

Ni-NTA resin (1 mL per liter cell culture) pre-equilibrated in solubilization buffer were added to the supernatant and shake for 2 h at 4°C. After incubation, the Ni-NTA resin was spun down and poured into a glass column, and then washed with 50 mL solubilization buffer. The heterotrimeric GoA was then gradually exchanged into E2 buffer (20 mM HEPES pH 7.5, 50 mM NaCl, 0.1% MNG, 1 mM $MgCl_2$, 5 mM beta-ME, 10 μM GDP, 2.5 μg ml^{-1} leupeptin and 160 μg ml^{-1} benzamidine). The protein was then wash with 50 mL E3 buffer (20 mM HEPES pH 7.5, 50 mM NaCl, 0.02% MNG, 1 mM $MgCl_2$, 5 mM beta-ME, 10 μM GDP, 2.5 μg ml^{-1} leupeptin and 160 μg ml^{-1} benzamidine) and eluted with E3 buffer supplemented with 250 mM imidazole.

The sample was then dephosphorylated by treating with 5 μL lamda phosphatase (supplement with 1 mM $MnCl_2$ for activity, New England Biolabs), 1 μL CIP (New England Biolabs) and 1 μL Antarctic phosphatase (New England Biolabs) and incubated at 4°C overnight. Meanwhile, the 6xHis-tag was removed using 3C protease. Cleaved GoA was purified by an additional negative Ni-NTA purification step. The Ni-NTA chromatography purified GoA was further purified with MonoQ column (GE Healthcare). The peak fractions of MonoQ column were collected and exchanged to E4 buffer (20 mM HEPES pH 7.5, 100 mM NaCl, 0.02% MNG, 1 mM $MgCl_2$, 10 μM GDP, 50 μM TCEP) by repeated concentration and dilution using a 50 kDa molecular weight cutoff Millipore concentrator. The concentrated heterotrimeric GoA was aliquoted, flash frozen in liquid nitrogen and frozen at −80°C before use.

GTPase-Glo™ assay

The unlabeled M2R for GTPase-Glo™ assay were expressed and purified as described above and frozen at −80°C before use. The GTPase reaction was initiated by mixing GoA and M2R in 5 μL reaction buffer (20 mM HEPES, 100 mM NaCl, 0.02% MNG, 1 mM $MgCl_2$, 5 μM GTP, 5 μM GDP, with or without 1 mM ligands) in a 384-well plate. Both GoA and M2R were fixed at a final concentration of 0.5 μM in the reaction system. For every independent experiment, GoA alone was set as a reference. The GTPase reaction was incubated at room temperature (22-25°C) for 2 h. After incubation, 5 μL reconstituted 1xGTPase-Glo™ Reagent (Promega) was added to the completed GTPase reaction, mixed briefly and incubated with shaking for 30 minutes at room temperature (22-25°C) to convert the remaining GTP into ATP. Then 10 μL Detection Reagent (Promega) was added to the system and incubated

CellPress

the 384-well plate for 5-10 minutes at room temperature (22-25°C) to convert the ATP into luminescent signals. Luminescence intensity was quantified using a Multimode Plate Reader (PerkinElmer) luminescence counter. Data were normalized to (acetylcholine (E_{max} %) and analyzed using GraphPad Prism 6.0.

NMR spectroscopy

The final NMR sample for M2R (∼250 μl) were loaded into the Shigemi microtubes (Shigemi Inc.) for data collection. D_2O was used for field lock and 2,2-dimethyl-2-silapentane-5-sulfonic acid (DSS) was used as the internal chemical shift reference. NMR data were collected at 25°C on a Burker Avance 800-MHz spectrometer equipped with a triple-resonance cryogenic probe. The ^{1}H-^{13}C heteronuclear single-quantum coherence (HSQC) spectra were recorded with spectral widths of 12820.5 Hz in the ^{1}H-dimension (w1) and 16077.2 Hz in the ^{13}C-dimension (w2) centered at 45 ppm in ^{13}C-dimension. For all spectra, 512 × 128 complex points were recorded and a relaxation delay of 2 s were inserted to allow spin to relax back to equilibrium. 56-80 scans gave rise to an acquisition time around 8-12 h for each spectrum depending on the sample concentration. All NMR spectra were processed using the software package NMRPipe/NMRDraw (Delaglio et al., 1995) and analyzed using the program NMRViewJ (Johnson and Blevins, 1994). The apo-state spectrum was collected by directly adding the concentrated sample into the Shigemi microtube. For ligands bound spectra, every ligand was added to the sample at concentrations of at least 10-fold stoichiometric excess over the receptor (around 1mM), and more than 10-fold over their Ki values to ensure that the receptors were fully occupied by the ligands. For iperoxo, acetylcholine and pilocarpine bound states, Nb9-8 was further added into the agonist bound sample at around 1.5:1 molar ratio and the HSQC spectra of agonist-receptor-Nb9-8 complex were collected.

Radio-ligand binding assay

For saturation binding studies, Sf9 membranes containing 50-100 femtomoles of receptor were incubated with increasing concentration of [^{3}H]-NMS at room temperature for 2 h in a buffer containing 20 mM Tris, 100 mM NaCl, 0.5% bovine serum albumin. Non-specific binding of the radioligand was determined by adding 10uM atropine in the same reaction system. For competition binding studies, Sf9 membranes were incubated with 2 nM [^{3}H]-NMS and increasing concentration of test ligand in the same buffer as saturation binding. Membranes were separated from excess [^{3}H]-NMS by Whatman GF/B filters using a Brandel 48-well harvester. The bound radioligand were read on a liquid scintillation counter (MicroBeta Jet, PerkinElmer). Data were analyzed by GraphPad Prism 6.0.

Molecular dynamics simulations

Simulations of active state M2R were based on the iperoxo bound crystal structure (PDB entry 4MQS). For the simulations of acetylcholine, carbachol and PR15 bound M2R, iperoxo was removed and the respective ligands were docked utilizing CCDC GOLD Suite v5.4.

Coordinates were prepared with UCSF Chimera (Pettersen et al., 2004). Missing side-chains were modeled, methionine mutations introduced to get the M2R$_\Delta$5M construct, hydrogens added, and chain termini capped with the neutral acetyl and methylamide groups.

All titratable residues were left in their dominant protonation state at pH 7.0. The protein structures were then aligned to the Orientation of Proteins in Membranes (OPM) (Lomize et al., 2006) active state structure of M2R (PDB entry 4MQS). Each complex was inserted into a pre-equilibrated membrane of dioleoyl-phosphatidylcholine (DOPC) lipids by means of the GROMACS tool g_membed (Wolf et al., 2010). Subsequently, sodium and chlorine ions were added to give a neutral system at 0.15 M NaCl. The final system dimensions were roughly 78 × 78 × 125 Å^3, containing 152 lipids 72 sodium ions, 70 chlorine ions and about 17.500 water molecules.

Parameter topology and coordinate files were build up using the tleap module of AMBER18 (Case et al., 2018) and subsequently converted into GROMACS input files. For all simulations, the general AMBER force field 2 (GAFF2) was used for ligands, the lipid14 force field (Dickson et al., 2014) for DOPC molecules and ff14SB (Maier et al., 2015) for the protein residues. The SPC/E water model (Bayly et al., 1993) was applied. Parameters for ligands were assigned using antechamber (Case et al., 2018). Structures of the ligands were optimized by means of Gaussian 09 (Frisch et al., 2010) at the B3LYP/6-31G(d) level, charges calculated at HF/6-31G(d) level and partial charges assigned according to the RESP procedure (Bayly et al., 1993). A formal charge of +1 was defined for all ligands.

Simulations were performed using GROMACS 2018.1 (Abraham et al., 2015; Van Der Spoel et al., 2005). The simulation systems were energy minimized and equilibrated in the NVT ensemble at 310 K for 1 ns followed by the NPT ensemble for 1 ns with harmonic restraints of 10.0 kcal·mol^{-1} on protein and ligands. In the NVT ensemble the V-rescale thermostat was used. In the NPT ensemble the Berendsen barostat, a surface tension of 22 dyn·cm^{-1}, and a compressibility of 4.5×10^{-5} bar^{-1} was applied. The system was further equilibrated for 18 ns with restraints on protein backbone and ligands. Multiple simulations were started from the final snapshot of the equilibration procedure resulting in productive molecular dynamics simulation runs of 3 × 2 μs for each simulation system. Simulations were performed using periodic boundary conditions and time step of 2 fs with bonds involving hydrogen constrained using LINCS. Long-range electrostatic interactions were computed using the particle mesh Ewald (PME) (Darden et al., 1993) method with interpolation of order 4 and FFT grid spacing of 1.6 Å. Non-bonded interactions were cut off at 12.0 Å.

The analysis of the trajectories was performed using the CPPTRAJ (Roe and Cheatham, 2013) module of AMBER18 and visualization was performed using the PyMOL Molecular Graphics System, Version 2.1.1 (Schrödinger, LLC). Distance and dihedrals were plotted using Matplotlib (Hunter, 2007).

G-protein IP-1 assay and β-arrestin recruitment assay

Determination of G-protein mediated M2R signaling was performed applying the IP-One HTRF® assay (Cisbio, Codolet, France) according to the manufacturer's protocol. In brief, HEK293 cells were grown to a confluence of approx. 70% and transiently co-transfected with the cDNA of the human M2R (cDNA Rescource Center, Bloomsberg, PA) and the hybrid G-protein G_{qi} (G_q protein with the last five amino acids at the C terminus replaced by the corresponding sequence of G_i; gift from The J. David Gladstone Institutes, San Francisco, CA) at a ratio of 1:7 applying Mirus TransIT-293 transfection reagent (Peqlab, Erlangen, Germany). Next day cells were detached from the culture dish with Versene (Life Technologies, Darmstadt, Germany), seeded into black 384-well plates (10000 cells/well) (Greiner Bio-One, Frickenhausen, Germany) and maintained for 24 h at 37°C. Agonist properties were determined by incubating the test compounds for 90 minutes at 37°C. Incubation was stopped by adding detection reagents (IP1-d2 conjugate and Anti-IP1 cryptate TB conjugate each dissolved in lysis buffer) for further 60 minutes at RT. Time resolved fluorescence resonance energy transfer (HTRF) was determined using the Clariostar plate reader (BMG, Ortenberg, Germany). Data analysis was performed by nonlinear regression using the algorithms for log(agonist) versus response of PRISM 6.0 (GraphPad, San Diego, CA) and normalization of the raw data to basal (0%) and the maximum effect of acetylcholine (100%). Concentration response curves from four to five individual experiments each done on duplicate are displayed as mean curve ± SEM.

Agonist properties mediated by M2R stimulated β-arrestin-2 signaling was determined applying the PathHunter® assay (DiscoverX, Birmingham, UK) as described in the manufacturer's protocol. In brief, HEK293 cells stably expressing the enzyme acceptor (EA) tagged β-arrestin-2 fusion protein were transiently transfected with the ProLink tagged flag-M2R-PKA construct and GRK2 (gift from M. Bouvier, IRIC University of Montreal, Canada) at ratio of 1:1 employing Mirus TransIT-293 transfection reagent. After one day cells were transferred into white clear bottom 384-well plates (5000 cells/well) (Greiner Bio-One) and maintained for further 24 h at 37°C. Test compounds dissolved in PBS were incubated for 150 minutes at 37°C. Stimulation was stopped by addition of detection mix and contued incubation for 60 minutes at room temperature. Chemiluminescence was determined using a Clariostar plate reader. Data analysis was done by nonlinear regression using the algorithms for log(agonist) versus response of PRISM 6.0 (GraphPad, San Diego, CA) and normalization of the raw data to basal (0%) and the maximum effect of acetylcholine (100%). Dose-response curves from seven to ten individual experiments each done on duplicate are displayed as mean curve ± SEM.

Calculation of signaling bias

Calculation of signaling bias parameters used the method as described (Namkung et al., 2016; van der Westhuizen et al., 2014). Briefly, data for each concentration response curve was analyzed by nonlinear regression using the operational model equation:

$$E = Basal + \frac{(E_m - Basal)}{1 + \left(\frac{\left(\frac{[A]}{10^{logK_A}} + 1\right)}{10^{logR} \times [A]}\right)^n}$$

In this equation, E is the effect of the ligand, E_m is the maximal possible response of the system, Basal is the basal level of response in the absence of agonist, [A] is the agonist concentration, $logK_A$ is the logarithm of the functional equilibrium dissociation constant of the agonist, n is the slope of the transducer function that links occupancy to response, and logR is the logarithm of the "transduction coefficient" τ / K_A.

To determine the logR values (equivalent to $log(\tau/K_A)$), data were first normalized as percentage of the maximal acetylcholine-stimulated response. For full agonists, the $logK_A$ is constrained to a value of zero (van der Westhuizen et al., 2014), whereas for partial agonists, $logK_A$ was estimated directly from curve fitting. Here, we defined PR15 and Iperoxo as full agonists for the G-protein IP-1 assay and only Iperoxo as the full agonist for the β-arrestin assay. For each assay, the basal was constrained to 0, while E_m and n were shared values determined by the non-linear regression. The logR values together with the standard errors were calculated then using the nonlinear curve fitting functions.

The $\Delta log(\tau/K_A)$ values were calculated by subtracting the $log(\tau/K_A)$ value of the reference ligand (here acetylcholine) in each pathway:

$$\triangle log\left(\frac{\tau}{K_A}\right) = log\left(\frac{\tau}{K_A}\right)_{ligand} - log\left(\frac{\tau}{K_A}\right)_{acetylcholine}$$

The standard error of $\Delta log(\tau/K_A)$ values were estimated using the following equation:

CellPress

$$SE_{\left(\triangle \log\left(\frac{\tau}{K_A}\right)\right)} = \sqrt{\left(SE_{\left(\log\left(\frac{\tau}{K_A}\right)\right)^{ligand}}\right)^2 + \left(SE_{\left(\log\left(\frac{\tau}{K_A}\right)\right)^{acetylcholine}}\right)^2}$$

Then, the $\Delta\Delta\log(\tau/K_A)$ values were calculated by subtracting the $\Delta\log(\tau/K_A)$ values for β-arrestin assay from $\Delta\log(\tau/K_A)$ values for Gqi assay for each ligand.

$$\triangle \triangle \log\left(\frac{\tau}{K_A}\right) = \triangle \log\left(\frac{\tau}{K_A}\right)_{ligand-Gqi} - \triangle \log\left(\frac{\tau}{K_A}\right)_{ligand-\beta Arr}$$

The standard error of $\Delta\Delta\log(\tau/K_A)$ values were estimated using equation:

$$SE_{\left(\triangle \triangle \log\left(\frac{\tau}{K_A}\right)\right)} = \sqrt{\left(SE_{\left(\triangle \log\left(\frac{\tau}{K_A}\right)\right)_{ligand.Gqi}}\right)^2 + \left(SE_{\left(\triangle \log\left(\frac{\tau}{K_A}\right)\right)_{ligand.\beta Arr}}\right)^2}$$

Finally, the ligand bias factors, relative to acetylcholine, were determined by taking the antilog of the $\Delta\Delta\log(\tau/K_A)$ (Kenakin et al., 2012).

Statistical analysis was performed using a two-tailed unpaired Student's t test on the $\Delta\log(\tau/K_A)$ ratios (mean, SEM, n) to make comparisons between two pathways (G-protein activation and β-arrestin recruitment) of for each ligand. $p < 0.05$ was considered to be statistically significant.

General materials and methods of organic synthesis

Dry solvents and reagents were of commercial quality and were used as purchased. High mass accuracy and resolution experiments were performed using mass spectrometer equipped with ESI-source and TOF-detector. IR spectra were performed on a Jasco FT/IR 4100 spectrometer (film on a NaCl crystal). Purification by flash chromatography was performed using Silica Gel 60 (40-63 μm mesh) from Merck as stationary phase; TLC analyses were performed using Merck 60 F254 aluminum sheets and the spots were visualized under UV light (254 nm) and with reagents such as $KMnO_4$ vapor. HPLC/MS was performed on a Thermo Scientific Dionex Ultimate 3000 HPLC system using DAD detection (230 nm; 254 nm) equipped with a Kinetex 2.6u mesh C8 100A (2.1 × 75 mm, 2.6 μm) HPLC column. Mass detection was performed with a BRUKER amaZon SL mass spectrometer using ESI ionization source. CHNS analytic was carried out on an elementar VarioMICRO cube with stearic acid as reference substance. NMR spectra were obtained on a Bruker Avance 400 (^{1}H at 400 MHz, ^{13}C at 100 MHz) or a Bruker Avance 600 (^{1}H at 600 MHz, ^{13}C at 150 MHz) spectrometer at 298 K using the solvents indicated. Chemical shifts are reported relative to TMS, acetone or to the residual solvent peak. The purity of all test compounds and key intermediates was determined by quantitative ^{1}H-NMR experiments using maleic acid as internal standard (calculated from three well-separated and specific signals). The following formula was used: $P_A = (I_A/I_{Mal}) \times (N_{Mal}/N_A) \times (M_A/M_{Mal}) \times (m_{Mal}/m_A) \times P_{Mal}$ (P, purity; I, integral area of the specific NMR signal; N, number of spins; M, molar mass; m, gravimetric weight of analyte (A) and maleic acid (Mal), respectively).

Synthetic procedures for PR15
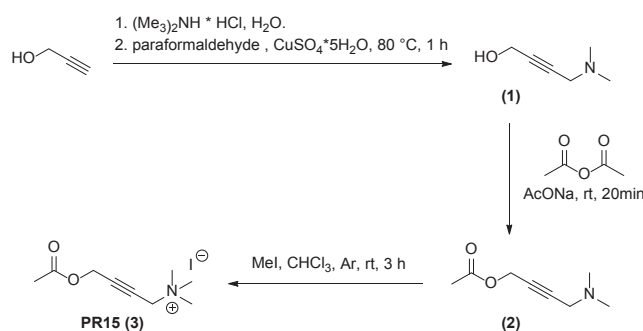
Scheme 1: PR15 (**3**) was synthesized starting from propargylic alcohol which was subjected to a Mannich reaction to give the tertiary amine **1**. Subsequent O-acetylation and N-methylation of the intermediate **1** resulted in formation of the product via the intermediate **2**.

CellPress

4-Dimethylaminobut-2-yn-1-ol (1) (Kloeckner et al., 2010)

To a solution of dimethylammonium hydrochloride (3 g, 46.06 mmol) in water (20 ml) was added 2 M aqueous NaOH solution to adjust the mixture to pH 9. Subsequently, paraformaldehyde (2 g, 24.57 mmol), 2-propyn-1-ol (2.4 g, 43.05 mmol) and a solution of $CuSO_4 \cdot 5\ H_2O$ (206 mg, 0.83 mmol in 2 mL water) were added and the pH value was set to pH 8 by adding 2M aqueous NaOH solution. The reaction mixture was stirred at 80°C for 1 h, allowed to cool to room temperature and poured into 20 mL of 25% aqueous ammonia solution. Continuous extraction over 72 h with methyl tert-butyl ether, drying of the organic layer over anhydrous Na_2SO_4 and evaporation of the solvent yielded **1** as a pale-yellow oil (1.15 g, 67%). ^{1}H NMR (400 MHz, DMSO-d_6): δ (ppm) = 5.14 (bs, 1H), 4.09 (s, 2H), 3.20 (t, J = 1.9 Hz, 2H), 2.16 (s, 6H); ^{13}C NMR (101 MHz, DMSO-d_6): δ (ppm) = 84.80, 79.10, 48.86, 47.21, 43.64; q-NMR (600 MHz, DMSO-d_6) Purity: 95%; HR-ESI-MS: calculated 114.0913, found 114,0904 $[M+H]^+$.

4-Dimethylaminobut-2-yn-1-yl acetate (2)
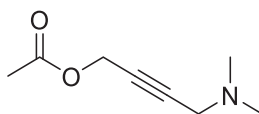
A solvent free mixture of **1** (500 mg, 4.4 mmol), acetic anhydride (677 mg, 6.63 mmol) and sodium acetate trihydrate (36 mg, 442 μmol) was stirred for 20 min at room temperature (Mojtahedi and Samadian, 2013). The mixture was diluted with methyl tert-butyl ether (20 ml) and washed with saturated $NaHCO_3$ solution (3 × 20 ml). The organic layer was dried over anhydrous Na_2SO_4 and concentrated under reduced pressure. Purification by column chromatography on silica gel (dichloromethane/ methanol/ aqueous ammonia (25%), 95:5:0.1) obtained **2** as a yellow oil (488 mg, 71%). ^{1}H NMR (400 MHz, CDCl₃): δ (ppm) = 4.72 (t, J = 1.9 Hz, 2H), 3.33 (t, J = 1.9 Hz, 2H), 2.33 (s, 6H), 2.10 (s, 3H). ^{13}C NMR (101 MHz, CDCl₃): δ (ppm) = 170.31, 82.12, 78.97, 52.44, 47.99, 44.18, 20.78; q-NMR (600 MHz, DMSO-d_6) Purity: 96%; HR-ESI-MS: calculated 156.1019, found 156.1012 $[M+H]^+$.

4-Acetoxy-N,N,N-trimethylbut-2-yn-1-aminium iodide, PR15 (3) (Jones et al., 1947)
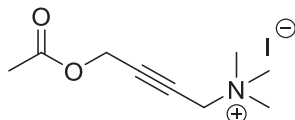
Iodomethane (91 mg, 640 μmol) was added dropwise to a solution of compound **2** (38 mg, 244.8 μmol) in dry chloroform (0.7 ml) under argon atmosphere. The mixture was stirred at room temperature for 3 h before surplus iodomethane and solvent was removed under vacuo. The residue was washed with methyl tert-butyl ether (3 × 5 ml) to give compound **3** as a white powder (57 mg, 79%). IR (NaCl): 3468, 3013, 2921, 2239, 1749, 1474, 1457, 1361; ^{1}H NMR (600 MHz, D₂O): δ (ppm) = 4.83 (s, 2H), 4.31 (s, 2H), 3.21 (s, 9H), 2.13 (s, 3H). ^{13}C NMR (151 MHz, D₂O): δ (ppm) = 173.96, 87.03, 74.95, 57.04, 53.36, 52.99, 49.37, 26.54, 20.77; q-NMR (600 MHz, DMSO-d_6) Purity: 99%; HR-ESI-MS: calculated 170.1176, found 170,11756 $[M]^+$; CHNS: calculated C 36.38%, H 5.43%, N 4.71%, S 0.0%, found C 36.43%, H 5.581%, N 4.72%, S 0.098%.